

# Recurrent Rossby waves ~~during Southeast and South-eastern~~ Australian heatwaves ~~and links to quasi-resonant amplification and atmospheric~~ ~~blocks~~

S. Mubashshir Ali\*<sup>1</sup>, Matthias Röthlisberger<sup>2</sup>, Tess Parker<sup>3</sup>, Kai Kornhuber<sup>4</sup>, and Olivia Martius<sup>1,5</sup>

1. Oeschger Centre for Climate Change Research and Institute of Geography, University of Bern, Bern, Switzerland,
2. Institute for Atmospheric and Climate Science, ETH Zürich, Zürich, Switzerland,
3. School of Earth, Atmosphere and Environment, Monash University, Clayton VIC, Australia,
4. Earth Institute, Columbia University, New York City, NY, USA, and
5. Mobiliar Lab for Natural Risks, University of Bern, Bern, Switzerland.

10 \*Corresponding author: mubashshir.ali@giub.unibe.ch

## Abstract

In the Northern Hemisphere, recurrence of transient Rossby wave packets over periods of days to weeks, termed RRWPs, may repeatedly create similar surface weather conditions. This recurrence leads to persistent surface anomalies ~~and high-impact weather events~~. Here, we first demonstrate the significance of RRWPs for persistent heatwaves ~~hot spells~~ in the Southern Hemisphere (SH). ~~We investigate) using the relationship between ERA-I reanalysis dataset and then examine the role of RRWPs, atmospheric blocking, and amplified quasi-stationary Rossby waves with two cases of heatwaves in Southeast blocks for heatwaves over south-eastern~~ Australia (SEA) in 2004 and 2009. This region has seen extraordinary heatwaves in recent years. ~~We also investigate the importance of transient systems such as RRWPs and two other persistent dynamical drivers: atmospheric blocks and quasi-resonant amplification (QRA).~~

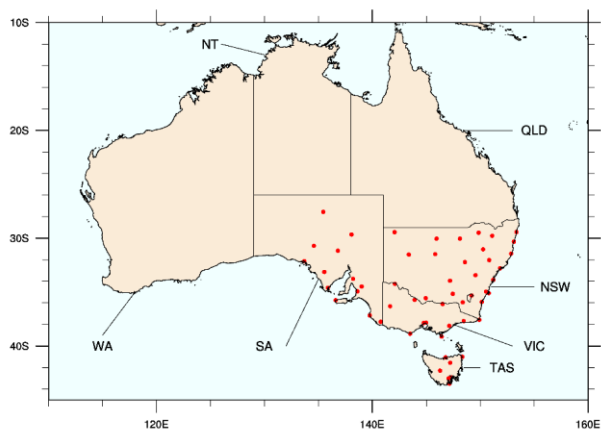
20 ~~We further explore the link between RRWPs, blocks, and QRA in the SH using the ERA-I reanalysis dataset (1979–2018). We find that QRA and RRWPs are strongly associated: 40% of QRA days feature RRWPs, and QRA events are 13 times more likely to occur with an RRWPs event than without it. Furthermore, days with QRA and RRWPs show high correlations in the composite mean fields of upper-level flows, indicating that both features have a similar hemispheric flow configuration. Blocking frequencies for QRA and RRWP conditions both increase over the south Pacific Ocean but differ substantially over parts of the south Atlantic and Indian Ocean. A Weibull regression analysis shows that RRWPs are~~

statistically associated with a significant increase in the duration of hot spells over several regions in the SH, including SEA. Two case studies of heatwaves in SEA in the summers of 2004 and 2009 illustrate the role of RRWPs in forming recurrent ridges (anticyclonic potential vorticity, PV anomalies), aiding in the persistence of the heatwaves. Then, using an observation-based dataset to identify SEA heatwaves, we find that SEA heatwaves are more frequent than climatology during days with extreme RRWPs activity. On days with both RRWPs and heatwaves, a circumglobal zonal wavenumber 4 anomaly pattern is present in the upper-level PV field, with an anticyclonic PV anomaly over SEA. In addition, we find positive blocking frequency anomalies over the Indian and the south Pacific Oceans, which may help to modulate the phase of RRWPs during SEA heatwaves.

## 1. Introduction

Since 1900, extreme heat has been responsible for more fatalities in Australia than all other natural hazards combined (Coates et al., 2014). Heatwaves also exacerbate the risk of wildfires, cause surges in power demand, and increase insurance costs (Hughes et al., 2020; Insurance Council of Australia, 2020). Increasingly frequent and severe heatwaves in the midlatitudes in the recent years (Coumou et al., 2013; Perkins-Kirkpatrick and Lewis, 2020; IPCC 2021) have spurred fruitful research on the atmospheric drivers of heatwaves. Understanding the dynamical mechanisms is particularly important for improving sub-seasonal prediction (Quandt et al., 2017) and for quantifying future changes in heatwaves (Shepherd, 2014; Wehrli et al., 2019; Shepherd, 2014). Several large-scale atmospheric mechanisms and phenomena have been identified as potential drivers of heatwaves in the Northern Hemisphere extra-tropics. These include blocking anticyclones (e.g., Barriopedro et al., 2011; Drouard and Woollings, 2018, Kautz et al., 2021), amplified quasi-stationary waves (Teng et al., 2016; Kornhuber et al., 2020), amplified Rossby wave patterns (e.g., Fragkoulidis et al., 2018; Kornhuber et al., 2020), and recurrent Rossby wave patterns (Röthlisberger et al., 2019). However, these phenomena have mainly been studied in isolation. Here, we focus on these three large-scale dynamical drivers of heatwaves to explore their relative importance, co-occurrence, and potential interactions during Fragkoulidis et al. (2018) showed that amplified Rossby waves are correlated with surface temperature extremes over NH and used process-based understanding to establish further association for the 2003 and 2010 NH heatwaves. RRWPs can be considered as a subset of amplified Rossby waves with a

50 condition that the transient eddies recur spatially in the same phase on a short time scale of days to weeks. Here, we focus on  
recurrent Rossby wave patterns to explore their importance for heatwaves in south-eastern Australia (SEA).



55 **Figure 1.** Map of Australia showing the states of SoutheastSouth-eastern Australia (SEA): South Australia (SA), Tasmania (TAS), Victoria (VIC), and New South Wales (NSW). Other states shown are Queensland (QLD), Northern Territory (NT), and Western Australia (WA). Red dots indicate Australian Bureau of Meteorology's (BoM) monitoring stations used in this study (see Methods).

Broadly, heatwaves in SEA (Fig. 1), comprising the states of Victoria (VIC), New South Wales (NSW), South Australia (SA), and Tasmania (TAS), are associated with slow-moving transient anticyclonic upper-level potential vorticity (PV) anomalies over the Tasman Sea (e.g., Marshall et al., 2013; Parker et al., 2014a; Quinting ~~et al.~~ and Reeder, 2017; Parker et al., 2019). The anticyclonic PV anomalies and the associated subsidence drive heatwaves over VIC (Parker et al., 2014b; Quinting ~~et al.~~ and Reeder, 2017). Several mechanisms can lead to the formation of These anticyclonic PV anomalies. One such mechanism is the excitation and propagation can form as a part of synoptic-scale Rossby wave ~~paekets~~packet (RWP) (King and Reeder, 2021). These RWPs are often initiated several days before the onset of the heatwaves, but they amplify, and eventually break over SEA as anticyclonic equatorward (LC1-type) Rossby wave breaking (Parker et al., 2014a; O'Brien and Reeder, 2017).

65 Surface temperature anomalies associated with transient RWP form, amplify, and decay ~~within~~ on synoptic timescales, but the recurrence of RWPs in the same phase on a sub-seasonal timescale can result in persistent surface weather conditions by repeatedly re-enforcing the surface temperature anomalies (e.g; Hoskins and Sardeshmukh, 1987; Davies, 2015). Röthlisberger et al. (2019) termed this phenomenon “Recurrent Rossby wave packets” (RRWPs) and demonstrated a statistically significant connection between RRWPs and ~~the~~ persistent ~~of~~ surface temperature anomalies ~~on a climatological~~

70 ~~timescale~~ in the Northern Hemisphere (NH). Ali et al. (2021) found that RRWPs are also associated with ~~persistent~~ ~~increased~~ ~~persistence of~~ dry and wet spells in several regions across the globe. ~~There is much to learn about mechanisms generating RRWPs and the interaction of RRWPs with other phenomena acting on different timescales.~~

~~Surface temperature anomalies in the extratropics are also well known to be associated with slow moving (stationary) blocking anticyclones. From a PV perspective, blocks are regions of anticyclonic PV anomalies in the upper troposphere~~

75 ~~large enough to disrupt the westerly jet stream and flanked by cyclonic PV anomalies (e.g., Hoskins et al., 1983; Schwierz et al., 2004; Nakamura and Hang, 2018). Blocks have been identified as a cause of major heatwaves in the NH midlatitudes (e.g., Black et al., 2004; Pfahl and Wernli, 2012; Schneidereit et al., 2012; Drouard and Woollings, 2018) because they lead to positive surface temperature anomalies due to clear sky conditions and subsidence mainly in the central part of the anticyclone (Trigo et al., 2004; Pfahl and Wernli, 2012).~~

80 ~~RRWPs and blocking anticyclones are closely linked. Röthlisberger et al. (2019, their Fig. 11) postulated three types of interactions between RRWPs and atmospheric blocking in the NH: blocking at the downstream end of an RRWP with the transient waves fuelling the block (Shutts, 1983); blocking acting as a metronome, setting up recurrent phasing of the waves downstream; and a combination of both mechanisms. Röthlisberger et al. (2019) showed that RRWPs often co-occur with blocking in the North Atlantic and North Pacific basins.~~

85 ~~Finally, quasi-stationary anticyclones, linked to amplified and longitudinally elongated Rossby waves, have also been observed in association with quasi-resonant wave amplification (QRA) events (Petoukhov et al., 2013). During QRA events, synoptic-scale free waves and forced waves interact, which non-linearly amplifies the wave amplitude (see Kornhuber et al., 2017a for more details on QRA). Based on the approximations of linear Rossby wave theory, the QRA framework has so far been tested with reanalysis data and currently awaits further validation from more idealized modelling frameworks (e.g.,~~

90 Mooring & Linz 2020). QRA conditions have been diagnosed for several recent heatwave events: the Russian heatwave of  
2010 (Petoukhov et al., 2013), and the heatwaves of summer 2018 in the NH midlatitudes (Kornhuber et al., 2019).  
Kornhuber et al. (2017b) presented evidence from reanalysis data for QRA of wavenumbers 4 and 5 in the Southern  
Hemisphere (SH). QRA is one of the mechanisms suggested to foster multiple simultaneous blocking events that are linked  
to slow-moving amplified Rossby waves of synoptic wavenumber ( $k \geq 5$ ) (Kornhuber et al., 2017a; Petoukhov et al., 2013).  
95 However, Wirth and Polster (2021) suggest an inverse causal link by which blocking could create the waveguide structures  
that are required to identify QRA conditions. The links and potential causality between QRA and blocking hence, remains an  
open question.

Transient high-frequency recurrent Rossby wave packets (RRWPs) have also been observed for some heatwave events  
linked to the QRA mechanism in the NH. The 1994 European heatwave identified as a QRA event in Kornhuber et al.  
100 (2017a) has also been identified as an RRWP event in Röthlisberger et al. (2019), and the Russian heatwave of 2010  
identified as a QRA event has been shown to be composed of RRWPs (see Fig. 10 in Fragkoulidis et al., 2018). The co-  
occurrence of QRA and RRWP in these cases suggests an organization of transient non-stationary wave packets during QRA  
conditions. The 7–15 day time filter applied in the QRA framework to define the background state might obscure a  
substructure that becomes apparent on sub-daily Hovmöller diagrams. However, the climatological frequency of co-  
105 occurrence of QRA and RRWPs is unknown, as are potential interactions between the two. Thus, studying the dynamical  
processes acting on weather timescales during QRA conditions is of interest to uncover the potential interactions with  
RRWPs.

The examples above highlight the need to assess how the transient features captured by the RRWP framework interact with  
stationary features, such as blocking and amplified Rossby waves that occur regionally or at a hemispheric scale. We  
110 investigate the link between these dynamical frameworks with a primary RRWP standpoint using co-occurrence and  
composite analyses. We use climatological datasets of blocking anticyclones (Schwierz et al., 2004; Rohrer et al., 2018),  
QRA conditions (Kornhuber et al., 2017b; Petoukhov et al., 2013), and RRWPs (Röthlisberger et al., 2019; Ali et al., 2021)  
to quantify the co-occurrence of the three features and mechanisms. The data sets also allow us to investigate some of the  
proposed causal links discussed above and summarized in Fig. 2.

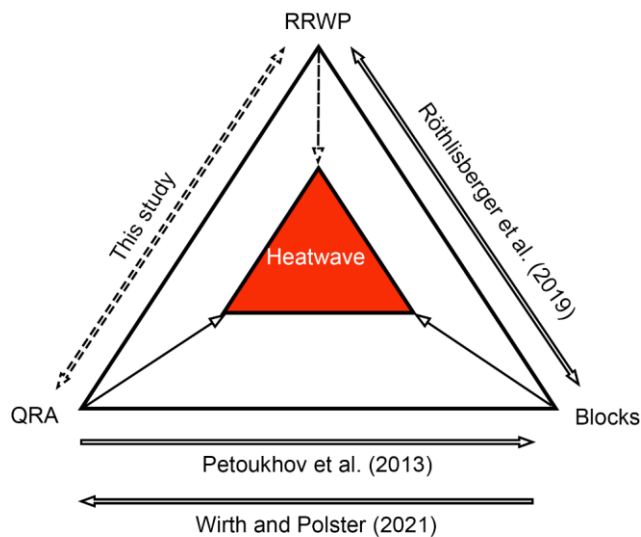


**Figure 2: Schematic summary of the links between QRA conditions, blocking, and RRWPs with heatwaves. Solid arrows indicate links reported in the literature, and dashed lines indicate unexplored links.**

This paper follows the following sequence: first, we extend Röthlisberger et al.'s (2019) analysis to study the relevance of RRWPs for persistent hot spells in the SH on a climatological time scale with a particular focus on SEA. We then focus on SEA heatwaves and study the co-occurrence of RRWPs, QRA, and blocks in two cases. Subsequently, we shift our attention to RRWPs, QRA, and blocks and investigate their interactions on a climatological scale. Thus, this paper addresses four research questions:

- Are RRWPs relevant for persistent hot spells in the SH and if so, in which regions?
- How do SH RRWPs relate to Australian heatwaves, and do QRA conditions and blocks play a role?
- How do RRWPs conditions relate to QRA conditions in the SH?
- How do RRWPs and QRA conditions relate to blocks in the SH?

130 However, at least for some impacts, it is not only the simple occurrence of an extreme, however one defines an extreme, but also the duration of the extreme event that is important. This study addresses that aspect for the temperature extremes in the SH. More precisely, we evaluate the hypothesis whether an increase in R-metric, a measure of RRWPs (Röthlisberger et al. 2019), is associated with an increase in spell duration of the surface-temperature extremes over SH. Furthermore, we show how SH RRWPs relate to the persistent and extreme SEA heatwaves and demonstrate their association with the help of two case studies for the 2004 and 2009 heatwaves.

## 2. Methods

### 135 2.1 Data

This study uses ERA-Interim (ERA-I) reanalysis data (Dee et al., 2011) provided by the European Centre for Medium-Range Weather Forecasts on a  $1^\circ \times 1^\circ$  spatial grid for 1979–2018. Various fields are used including horizontal velocity, meridional velocity, 2 m temperature, PV, and sea surface temperature (SST). The datasets are freely available to download from <https://apps.ecmwf.int/datasets/data/interim-full-daily/levtype=pl/>. ~~Note that~~The PV fields in the SH are multiplied by a  
140 factor of -1. The climatological mean is calculated with respect to the period 1980–2010.

### 2.1 Recurrent Rossby Waves

The metric  $R_s$  developed by Röthlisberger et al. (2019) is used identify recurrence of synoptic-scale Rossby wave patterns. For the SH, we use the same metric as in Ali et al. (2021). First, a 14.25 day running mean of meridional velocity fields ( $\hat{v}_{rf}(\lambda, t)$ ), averaged between  $35^\circ$  S and  $65^\circ$  S, are calculated to isolate signals with timescales longer than the synoptic  
145 timescale for each longitude  $\lambda$  and time  $t$ . The envelope of the synoptic wavenumber contribution to the time-filtered  $v$  is extracted following Zimin et al., (2003). To do this, the time-filtered  $v$  fields are transformed into the frequency domain using a fast Fourier transform over longitude,  $\hat{v}_{rf}(k, t)$ . Finally, an inverse Fourier transform is applied to calculate the

envelope of the wave while only considering contributions from a selected band of synoptic wavenumbers  $k = 4-15$ . Thus,  $R(\lambda, t)$  for each longitude  $\lambda$  and time  $t$  is calculated as

$$R(\lambda, t) = \left| \sum_{k=4}^{k=15} \hat{v}_{\ell_f}(k, t) e^{2\pi i k l_\lambda / N} \right| \left| 2 \sum_{k=4}^{k=15} \hat{v}_{\ell_f}(k, t) e^{2\pi i k l_\lambda / N} \right| \quad (1)$$

where  $k$  is the wavenumber,  $l_\lambda$  denotes the longitudinal grid point index for longitude  $\lambda$  and  $N = 360$  denotes the number of longitudinal grid points.

In most cases, large values of  $R$  reliably identify situations in which amplified waves (of distinct wave packets) recur in the same phase. However, the definition of  $R$  does not contain criterion for recurrence of distinct wave packets. Thus, in a few cases, high values of  $R$  over a few days may result from stationary synoptic-scale troughs or ridges (see R othlisberger et al. 2019 for discussion on metric  $R$ ). Fig. A1 shows day-of-year climatology of the  $R$  metric in the Southern Hemisphere and compares it to that of the Northern Hemisphere.

High  $R$  days are defined as days on which the zonal mean  $R$  is greater than the 85<sup>th</sup> percentile. The code for calculating  $R$  metric is freely available (check Code and data availability section).

Phase and amplitude information of a particular wavenumber  $k$  can also be extracted using the same technique as in (1) and presented by Zimin et al. (2003). After applying the inverse Fourier transform, a complex number of the form  $a + ib$  is obtained. For extracting the wave packet or envelop, the amplitude of the complex number is taken as shown in (1). Instead of that, plotting the complex number on a complex plain provides information on the phase and amplitude at a given time step  $t$  for a particular wavenumber  $k$ . This is used to obtain a phase-amplitude distribution shown later.

## 2.2 Atmospheric blocks

Atmospheric blocks are identified from persistent anticyclonic PV anomalies averaged between 500 hPa and 150 hPa vertical levels with the detection scheme described in Schwierz et al. (2004) as updated by Rohrer et al. (2018). The code used is available on GitHub (<https://github.com/marco-rohrer/TM2D>). The detection scheme uses a 1.3 PVU threshold, a persistence criterion of 5 days, and a minimum overlap of 0.7 between two timesteps. Blocking fields identified with this algorithm are available at 6 hourly temporal resolution and  $1^\circ \times 1^\circ$  spatial resolution. ~~Blocking fields are resampled into~~



~~daily fields for further analysis.~~ We tested the sensitivity of the blocking fields with a 1.0 PVU threshold for the two case studies ~~and did not find blocking directly over SEA.~~

### 2.3 QRA data

175 QRA events are identified using the QRA detection scheme described in Kornhuber et al. (2017a), based on ERA-1 daily fields for December to February 1979–2018 at a spatial resolution of  $2.5^\circ \times 2.5^\circ$ , smoothed using a 15-day running mean. The detection scheme tests climate data for the resonance conditions defined by Petoukhov et al. (2013): the formation of a wave guide in the zonally averaged zonal wind field for a wavenumber  $k$  and the emergence of a forcing pattern of wavenumber  $m \approx k$ . Please refer to Kornhuber et al. (2017a) and Kornhuber et al. (2017b) for more details. For the co-  
180 occurrence analysis and the composites, we use the period of December to February 1979–2018, for which QRA data is available. For simplicity, days with QRA conditions are referred to as QRA days and those without as non-QRA days. 819 days out of 3520 days show QRA conditions, 576 of which show QRA with wavenumber 4.

Note: Here, QRA implies that the condition of waveguide and forcing is fulfilled and a high amplitude wave is observed.

### 2.4 Southeast/South-eastern Australian Heatwaves

185 A station-based heatwave dataset is used to focus on extreme and persistent heatwaves in SEA to study the links between RRWPs, blocks, and QRA conditions. Following the methods developed in Parker et al. (2014a) and refined in Quinting et al. and Reeder (2017), heatwaves in SEA in December–February (DJF) are detected from temperatures observed at the Australian Bureau of Meteorology’s (BoM) monitoring stations (Fig. 1). The BoM’s Australian Climate Observations Reference Network – Surface Air Temperature (ACORN-SAT, available at <http://www.bom.gov.au/climate/data/acorn-sat/#tabs=ACORN%E2%80%90SAT>) is a high-quality temperature dataset used to monitor long-term temperature trends.  
190 The dataset provides a daily maximum temperature (TMAX) for each station. These TMAXs are extracted for stations in SEA as defined here, for DJF from 1979 to 2019. The 90<sup>th</sup> percentile TMAX (T90) is then calculated for each station for each month in DJF. A heatwave is defined as any period of at least four consecutive days for which the TMAXs at three or more of these stations equal or exceed the T90 for that station and month. From here on, the term “heatwave” refers to heatwave in

195 SEA. ~~This criterion results in 58 heatwaves, which were on an average 8 days long with the longest 22 days~~ This criterion  
results in 57 heatwaves, which were on an average 8 days long with the longest heatwave lasting 22 days. Note that the  
purpose of the heatwave identification scheme is to identify the most intense and most persistent heatwaves in SEA, and thus  
serves a different purpose than the hot spell identification scheme described in the next section. Following Parker et al.  
2014a, a day part of the SEA heatwaves is termed as SEA heat day. For evaluating the co-occurrence of SEA HD with  
200 RRWP conditions, high  $R_{SEA}$  days are defined as days exceeding the 90<sup>th</sup> percentile of the daily mean  $R$  averaged over SEA  
(between 130° E and 153° E). The 90<sup>th</sup> percentile threshold is a subjectively chosen threshold consistent with the threshold  
for TMAX. Sensitivity test with a threshold of 85<sup>th</sup> percentile did not change the conditional probability shown in section  
3.3.

Formatted: Font color: Auto

## 2.54 Hot spells in the SH

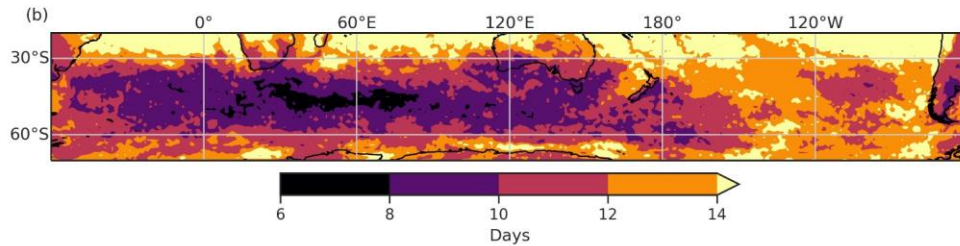
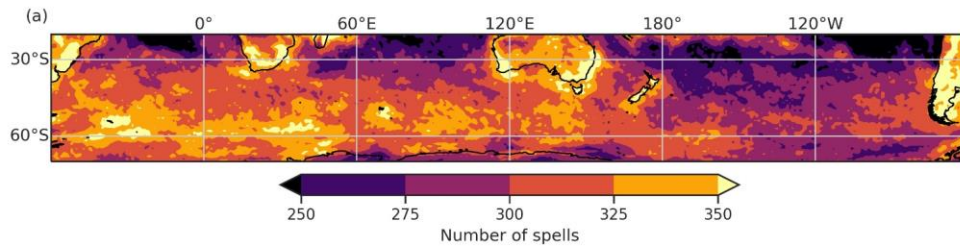
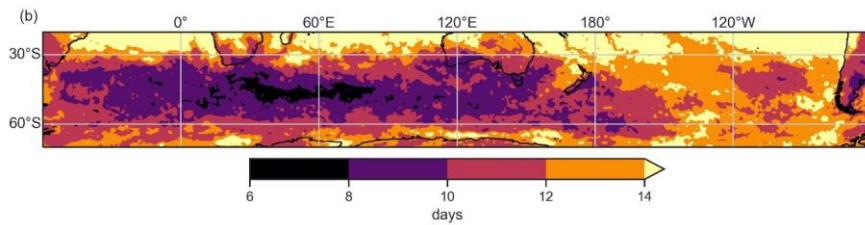
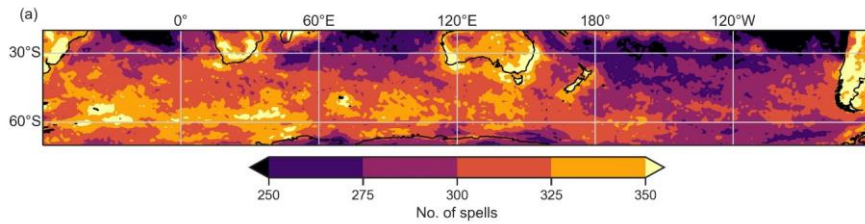


Figure 32: (a) Total number of hot spells in November–April identified at each grid point between 20° S and 70° S. (b) The 95<sup>th</sup> percentile of hot spell durations.

Formatted: Line spacing: single

Hot spells are identified for all SH grid points between 20°S and 70°S for 1980–2016 using 2 metre temperatures (T2M) from the ERA-I fields at 6 hourly temporal resolution and 1-degree spatial resolution between 20°S and 70°S are used to identify hot spell durations for 1980–2016. The hot spells definition follows that of Röthlisberger et al. (2019), in which a hot spell is calculated for each grid point as consecutive values exceeding the 85<sup>th</sup> percentile from the linearly detrended T2M fields. Spells separated by less than a day are merged to form a single uninterrupted spell. Spell durations of less than 36 hours are excluded from further analysis. We identify hot spells for the period of November to April as this allows longer spells, which are required for the model to work. Figure 3a Contrary to the SEA heatwave identification scheme, the purpose of the hot spell identification scheme is to identify many (not necessarily overly extreme) warm periods at each grid point, which can then be used for statistical analyses of the factors that determine the duration of these events. This statistical analysis (see next section) will be used to quantify the effect of RRWPs on the persistence of warm surface weather. To ensure a large sample size for robust statistical results, we identify hot spells for the period of November to April. Figure 2a shows the spatial distribution of the number of hot spells at each grid point between 20° S and 70° S. Higher number of hot spells are seen over land where parts of SEA, South Africa, and South America show 350 or more spells. The 95<sup>th</sup> percentile for hot spell duration varies from 6 days to more than 2 weeks (Fig. 3b2b). Over SEA, the 95<sup>th</sup> percentile duration varies from a week to roughly 2 weeks.

#### 2.6.5 Weibull regression model to assess the effect of RRWPs in the SH hot spells

We extend the analysis of To quantify the effect of RRWPs on the persistence of hot spell durations surface weather, we extend an analysis from Röthlisberger et al. (2019) to the SH, including SEA, using the same statistical model setup, a Weibull regression model. This model allows us to model the distribution of the duration of the hot spells at each grid point as opposed to classifying binary information about the occurrence of heatwaves (e.g., over SEA) based on a predictor (e.g., RRWPs). Another An advantage of Röthlisberger et al.'s (2019) model is that we do not need to subjectively define the duration of a significant spell because the model accounts for the assessment of changes in all quantiles of the spell duration modelled. The null hypothesis tested here is that RRWPs have no effect on the duration of hot spells, which is tested at each

[grid point](#). The Weibull model is only briefly introduced here. Please refer to R othlisberger et al. (2019) for further details and their [Supporting Information](#) for a detailed introduction to the Weibull model.

To fit the Weibull model to the observed spell duration, a representative value of the R-metric needs to be assigned to each hot spell. This is achieved in the following way: for each hot spell  $i$  at grid point  $g$  with a duration  $D_{g,i}$ , the raw R-metric  $R(\lambda, t)$  is longitudinally averaged within a  $60^\circ$  longitudinal sector centred at the grid point  $g$  with longitude  $\lambda_g$  to yield  $R_{lon}(\lambda, t)$ . Then, a median of  $R_{lon}(\lambda, t)$  is calculated for the lifetime of the hot spell to assign a representative value of  $R$  ( $\tilde{R}_{\lambda_g,i}$ ) for each spell. Thus, our model is given as (see R othlisberger et al., 2019 for further details):

$$\ln(D_{g,i}) = \alpha_{0,g} + \alpha_{1,g} \tilde{R}_{\lambda_g,i} + \sum_{j=2}^6 \alpha_{j,g} m_j(t_{g,i}^{start}) + \sigma_g \epsilon_{g,i} \quad ; i = 1, \dots, n_g. \quad (2)$$

Hereby  $\alpha_{0,g}$  is the intercept,  $\alpha_{1,g}$  is the regression coefficient for  $\tilde{R}_{\lambda_g}$  and the  $\alpha_{j,g}$  are regression coefficients for dummy variables  $m_j(t_{g,i}^{start})$  that take the value 1 if spell  $i$  starts in month  $m_j$ , and zero otherwise. The coefficients  $\alpha_{j,g}$  therefore, account for possible seasonality in the spell duration distribution at grid point  $g$  (e.g., longer hot spells in May compared to, e.g., September), while  $\sigma_g$  is a scale parameter and the  $\epsilon_{g,i}$  are error terms. The quantity  $\exp(\alpha_1)$  is usually referred to as acceleration factor ( $AF$ ) and is of particular interest here, as it quantifies the factor of change in all quantiles of the distribution of spell duration at grid point  $g$  per unit increase in  $\tilde{R}$  (Hosmer et al., 2008; Zhang, 2016; R othlisberger et al., 2019). An  $AF > 1$  implies an increase in all spell duration quantiles with increasing  $\tilde{R}$  (i.e., during RRWPs), and conversely for an  $AF < 1$ . Furthermore, fitting the model (2) to spell durations at all grid points thus results in a spatial field of  $AF$ . The statistical significance of the  $AF$  values is evaluated in a two-step approach. First, a p-value for the above null hypothesis is computed exactly as in Zhang (2016). Then, the false-discovery-rate (FDR) test of Benjamini and Hochberg, (1995) is applied to the resulting field of p-values. The FDR test controls for type I errors, i.e., falsely rejecting null hypothesis that can occur substantially in analyses like this one where multiple tests are being performed independently from each other at each grid point (e.g., Wilks 2016). Here we follow the recommendation of Wilks (2016) and allow for a maximum false-discovery-rate  $\alpha_{FDR}$  of 0.1.

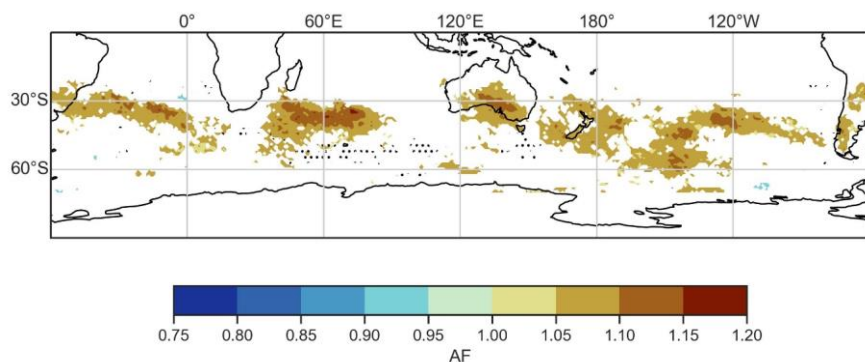
This model is fitted to durations of hot spells at each grid point. It results in a spatial field of regression coefficients  $\alpha_{j,g}$ ,  $j =$   
255  $0, \dots, 6$ , together with their  $p$  values. Here,  $\alpha_{1,g}$  represents the effect of  $\bar{R}$  on the hot spell duration. The  $\exp(\alpha_1)$ , referred to  
as the acceleration factor ( $AF$ ), corresponds to the factor of change in all quantiles of the spell duration  $D$  per unit increase in  
 $\bar{R}$  (Hosmer et al., 2008; Röthlisberger et al., 2019; Zhang, 2016). Statistical significance of  $AF$  is evaluated ~~by applying after~~  
~~controlling~~ the false discovery rate (FDR) ~~test of (Benjamini and Hochberg (1995) at maximum FDR 0.1 as in~~  
~~Röthlisberger et al. (2019), for type I errors due to falsely rejecting null hypothesis in multiple independent tests by setting~~  
260 ~~the FDR threshold,  $\alpha_{FDR}$  to 0.1 as recommended by Wilk's (2016).~~ Thus, regions with  $AF > 1$  ( $AF < 1$ ) experience an increase  
(decrease) in spell duration with increasing (decreasing)  $R$ .

### **2.7 Controlling False Discovery Rate (FDR)**

~~We use Benjamini and Hochberg's (1995) procedure to control for type I errors due to falsely rejecting the null hypothesis in~~  
~~multiple independent tests. For the statistical tests used in the composite analysis, the FDR threshold,  $\alpha_{FDR}$  is set to 0.1,~~  
265 ~~where FDR is the expected ratio of the number of false positive discoveries to the total number of discoveries: rejection of~~  
~~the null hypothesis. We choose  $\alpha_{FDR}$  as  $\alpha_{FDR} = 2\alpha_{global}$  as per Wilks's (2016) recommendation, where  $\alpha_{global} = 0.05$  is~~  
~~the significance level chosen for the statistical tests in the composite analysis.~~

## **3. Results**

### **3.1 Climatological effect of RRWPs on and hot spell duration in Australia durations**



270 **Figure 43:** Statistically significant acceleration factors (AF) for hot spells in November–April between 20° S and 70° S. Colours show AFs from a Weibull model with R metric as a covariate. Stippling indicates areasgrid points where spell duration  
 275 doesdurations do not follow the Weibull model based on the Anderson–Darling test at a significance level of 0.01.

275 The Weibull analysis reveals that RRWPs have a significant effect onare significantly correlated with the duration of hot spells in several regions within the SH and in-particular-including over SEA (Fig. 43). Recall that AF >larger than 1 (AF <-1) means that an increase or-decrease in R is related to an increase or-decrease in hot spell duration, respectively, and conversely for AF smaller than 1. Thus, several parts of central and southern Australia, including the states of SA, VIC, NSW, and TAS, experience longer hot spells during periods when RRWPs occur. Interestingly, Northern Australia, however, does not show such an-associationa correlation with RRWPs, which agrees with previous studies showing different dynamical pathways for Northern and Southern Australian heatwaves (Risbey et al., 2017; Quinting and Reeder, 2017; Parker et al., 2019; Quinting et al., 2017). Other statistically significant areas over land include parts of South America: southern Brazil, Bolivia, and parts of Argentina and Chile. The AFs in Fig. 4 alsoFor Northern Hemisphere summer half-year, the significant AFs, larger than 1, form a wavenumber 4 spatial7 pattern, in contrast to the wavenumber 7-8 pattern in the NH summer half year (MJJASO) seen in- (Röthlisberger et al. (., 2019). However, the presence of aIn contrast, no clear  
 285 wave pattern emerges for the SH in the significant AFs in Fig. 3. The difference in AF patterns between the two hemispheres is consistent with different climatological stationary wave patterns. The spatial pattern does-not-necessarily-indicate-the existence-of-a-dominant-circumhemispheric-wave-during-RRWPs. It-merely-in Figure 3 highlights areas where the transient

Formatted: English (United Kingdom)

Formatted: English (United Kingdom)

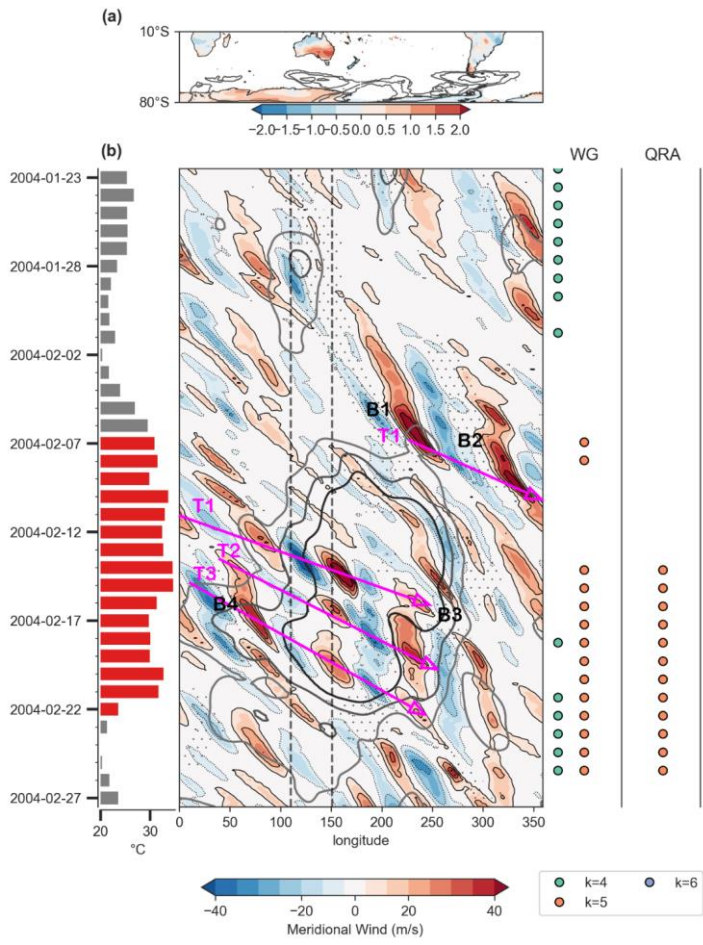
waves building up the RRWPs have a predominant phasing. ~~The~~ in summer. In summary, the regression analysis shows that RRWPs are ~~an important feature in the SH as well: RRWPs increases~~ significantly associated with the duration of hot spells  
290 in several SH regions over land, including SEA; ~~however,~~ However, the Weibull analysis does not provide any information about ~~how frequently RRWPs and the processes and hence potential causal link between RRWPs and the most intense SEA heatwaves coincide.~~ Accordingly, we next focus on SEA heatwaves ~~using an observation-based dataset and quantify the simultaneous presence of RRWPs, QRA conditions, and atmospheric blocking~~ and elucidate the role of RRWPs and blocks for two selected cases studies of SEA heatwaves and investigate further co-occurrence of SEA heatwaves and days with high  
295 R activity.

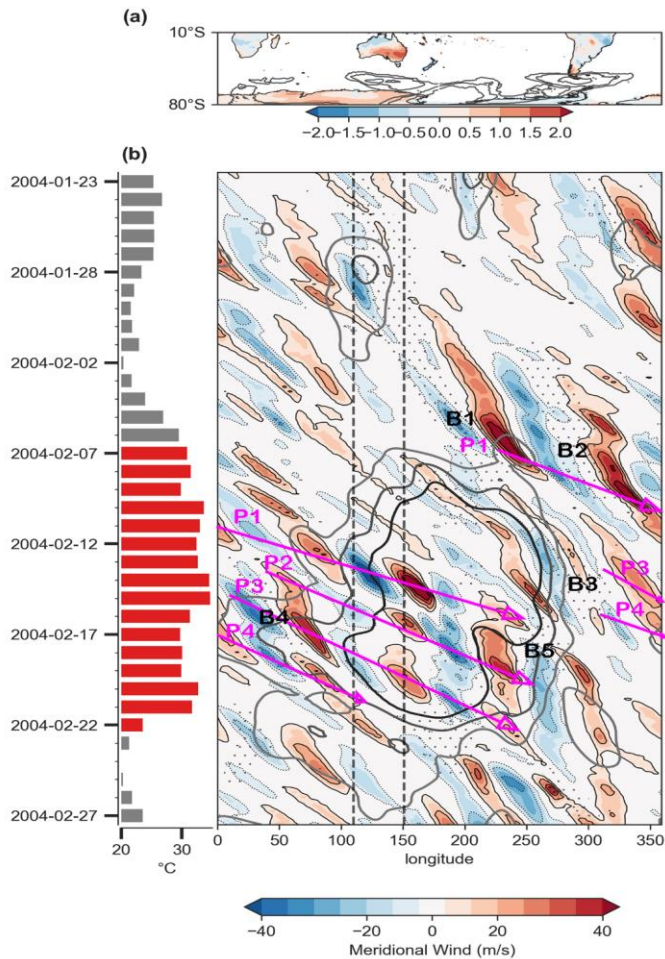
### 3.2 RRWPs, Blocks, and QRA during two extreme and persistent SEA heatwaves

#### 3.2.1 Case 1: 2004 Heatwave

The February 2004 heatwave (7–22 February) lasted for 16 days. More than 60% of continental Australia recorded temperatures above 39°C during this event (National Climate Centre, 2004). At the time, this event was the most severe  
300 February heatwave on record in both spatial and temporal extent and ranked in the top five Australian heatwaves for any month (National Climate Centre, 2004). More than 100 stations in SA, NSW, and northern VIC experienced record temperatures for February, and in some regions all-time records were set for consecutive days of heat (BoM, 2004). Previous studies have shown that the upper-level anticyclonic PV anomalies over SEA during the heatwaves are associated with subsidence and is the major process causing the high surface temperature anomalies (e.g., Quinting and Reeder, 2017; Parker et al., 2019). The surface flow associated with anticyclonic anomalies may also advect warm continental air due to the north westerly flow at lower levels (e.g., Parker et. al. 2014b). Here, we show how RRWPs contribute to persistent anticyclonic PV anomalies over SEA.  
305



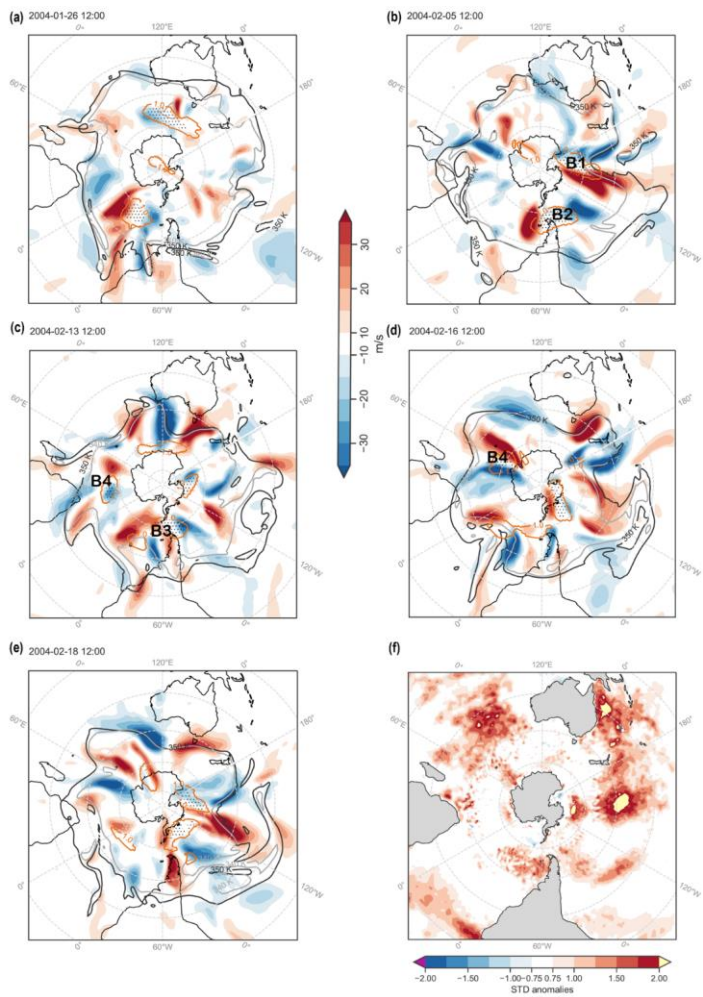


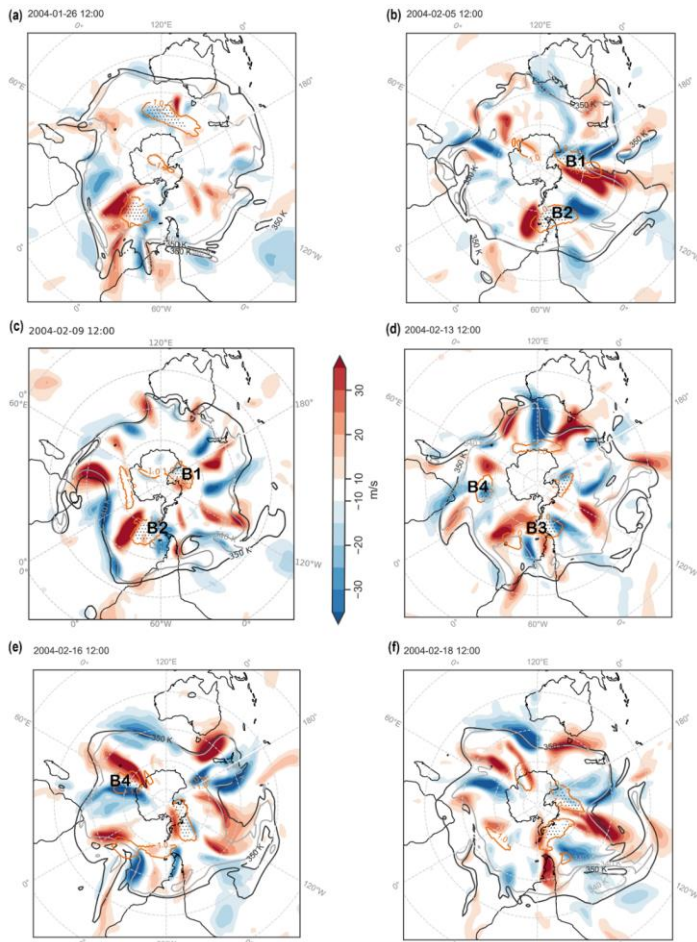


310 Figure 54: RRWPs, and blocks, and QRA conditions during 2004 SEA heatwave. (a) Filled contours depict the time-mean-of  
 315 standardized anomalies of daily maximum 2 m temperature over land for the duration of the heatwave. Contours show the mean  
 blocking frequency during the heatwave (5, 10, 20%). (b) Bars show daily maximum 2 m temperature averaged over  
 SEA (°C); red marks the heatwave period. The Hovmöller diagram shows the meridional wind at 250 hPa averaged between 35° S  
 and 65° S (filled contours, m/s),  $R$  values (grey contours, 6, 8, 10 m/s), and longitudes at which at least one grid point between 40° S  
 and 70° S featured an atmospheric block (stippling). Rossby wave trains (blocks) are labelled in black.

The right columns in (b) indicate the presence of waveguides and quasi-resonance amplification conditions, with coloured dots indicating the wavenumber (see legend).

Formatted: English (United Kingdom)





320 **Figure 6S:** (a), (b), (c), (d), (e), and (f) show meridional velocity at 250 hPa (colour shading), 2 PVU contours at isentropes 340 K (black line) and 350 K (grey line) at various time steps. Stippling and orange contours show blocks identified using a 1.3 and 1.0 PVU threshold, respectively. (f) shows standardized SST anomalies with respect to austral summer (DJF) climatology for heatwave days, including the 10 days prior to the heatwaves (27 January–22 February).

325 ~~During this event, several Rossby wave packets were observed, recurrently amplifying in the same phase forming a ridge over SEA. The upper-level flow over SEA was highly non-linear upstream of South America in the Pacific basin before the onset of the heatwave. On 26 January 2004, zonal prior to the onset, a split jet structure was associated with a block south of Australia, where the subtropical branch of the jet was located over SEA heatwave (Fig. 6a). On 30 January, an anticyclonic wave breaking (AWB) event occurred upstream of Australia in the Indian Ocean at  $\sim 100^\circ$  E. A further AWB event took~~  
330 ~~place on 3–5a). An upper-level ridge forms over SEA around 5 February prior to the heatwave (Fig. 5b) over SEA. The PV fluxes associated with the~~The flow becomes more amplified in the subsequent days with a circumglobal amplified wave breaking helped to shift the jet southward over the Tasman Sea and in the formation of the first ridge (Fig. pattern apparent around  
335 ~~6b). The flow over Australia became zonal again on 7 February and remained so until 9 February, when a short- (Fig. 5c). The amplified wave ridge passed over SEA (not shown). On 10 February, AWB over western Australia resulted in the amplification of a subsynoptic to synoptic scale ridge downstream over SEA, and a large-scale AWB over the southern Indian Ocean ( $\sim 30^\circ$  E) led to the formation of a downstream ridge across most of the southeastern Indian Ocean. Simultaneously, the sea surface temperatures (SSTs) were anomalously warm in the Indian Ocean. In fact, SSTs were anomalously high in several parts of the SH, including parts of the Pacific and the Atlantic Ocean for the whole duration of the heat, part of a transient and nonstationary Rossby wave as well as 10 days prior to the onset of the heatwave (Fig. 6f).~~  
340 ~~Next, a synoptic-scale wavepacket, RWP (P1 in Fig. 4b), arrived over the southern Indian Ocean, and an upper-level ridge began to form over Australia on 12 February as part of a transient and nonstationary RWT (T1 in Fig. which amplified further around~~5b). On 13 February, conditions for quasi-resonance were met for wavenumber 5 (Fig. 5b), which may have led to the amplified waves around most of the Southern Hemisphere (Fig. 6e, 6d). 5c). Two further ridges formed over SEA on 16 and 18 February (Fig. 6e, 6d 5e, 5f), each ridge being part of a transient nonstationary RWT. This RWP initiated  
345 ~~upstream of Australia (P3, P4 in Fig 5b). These series of upper-level recurrent ridges were~~part of the RRWPs and contributed to the persistence of the heatwave. These recurrent ridges associated with RRWPs were also detected by the metric  $R$  (grey contours in Fig. 5b). By 20 February, the flow had returned to zonal over SEA, but a split jet formed over SEA by 22 February. 4b).

No blocks were identified directly over SEA during the heatwave, but blocks were present south of SEA and further downstream (Fig. 4, 5, 6). The ~~RWTRWP~~ labelled as ~~T1P1~~ in ~~Fig-Figure~~ 5b formed downstream of a block (~~B1 in Fig-~~ downstream of Australia where the block moved from south of Australia a few days earlier (Fig. 5b)-south). Another block ~~B2~~ was simultaneously present in the vicinity of South America around 7 February. ~~Another RWT (T2 in Fig. 5b)~~In the next few days, simultaneous wave breaking was observed in the central Pacific Ocean and south of Africa in the Indian Ocean. ~~Another set of RWPs (P3 and P4 in Fig. 4b)~~ seems to have been set off by a block over the ~~IndianPacific~~ Ocean (~~B4B3~~ in Fig. 5b). Simultaneously, another block was present south of South America (~~B2B4~~ in Fig. 5b, 6d4b, 5d), and ~~they~~ seem to ~~set-off~~initiate another RWT (~~T3RWP (P3~~ in Fig. 5b4b). Block B4 ~~was also~~ resulted in the amplification of the associated with amplified Rossby ~~wave-waves downstream~~ over the Indian Ocean on 16 February (Fig. 6d5d). Thus, we argue that blocks could have played a key role in the initiating, phasing, and meridional amplification of the three Rossby wave ~~trains~~ (~~T1-T3~~packets (P1-P4) that reached Australia between 13 and 18 February. In summary, we saw ~~three RWTs~~recurring ~~RWPs~~ that passed over Australia during ~~the QRA~~this period (Fig. 5b4b). These waves were not stationary, they were not triggered in the same area, and ~~they~~not over Australia, and were ~~initially~~ not in phase upstream of Australia.

### 3.2.2 Case 2: 2009 Heatwave

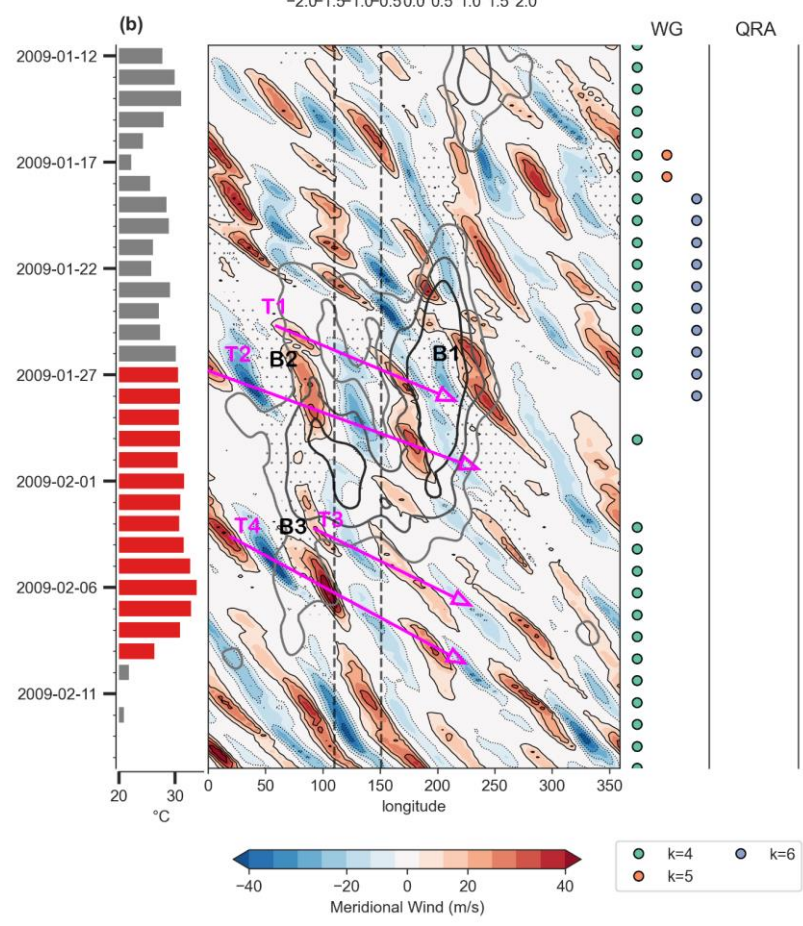
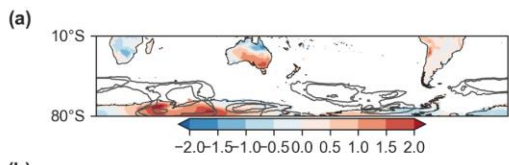
The 2009 heatwave (27 January–9 February), although extensively covered in literature (e.g., Engel et al. 2013, Parker et al. 2014b), has been chosen because it is one of the most severe heatwaves in SEA. It lasted for 14 days. ~~During~~Between 28–31 January and 6–8 February, temperatures in SEA were exceptionally high. On Black Saturday, 7 February, the hot, dry, and windy conditions worsened many catastrophic fires in VIC, which recorded 173 fatalities, and more than 2133 houses were destroyed (Karoly 2009; Parker et al., 2014b; VBRC 2010). ~~During this heatwave, an anticyclone over SEA and the associated north-westerly flow at the surface advected hot continental air into SEA leading to extreme surface temperatures~~ (Parker et al., 2014b).

Prior to the onset of the heatwave, the ~~large-scale upper-level~~flow was ~~highly non-linear, with several basin-wide AWB events in the south Pacific and south Atlantic similar to the 2004 heatwave. However, unlike the 2004 heatwave, the flow was not zonal over SEA prior to the heatwave, with an AWB occurring on 17 January over SEA in association with a block~~

present upstream over the South Atlantic. A hemisphere-wide already amplified with a wave breaking over SEA (Fig. 7a). Several RRWPs were observed prior to and during this event (P1 and P2 in Fig. 6b). Rossby wave was present during 17–19 January (Fig. 7b); however, the forcing conditions for QRA were not met.

RRWPs occurred from 26 January onwards with the RRWPs prior to the heatwave were not in the same phase as those during the heatwave (Fig. 6b). Around 26 January, a Rossby wave packet (P2 in Fig 6b) was observed forming an upper-level ridge forming over Australia (Fig. 7b, 8b). An AWB occurred over SEA (Fig. 6b, 7b). In the subsequent days, the amplified wave broke anticyclonically over SEA (Fig. 7c), resulting in an anticyclonic PV anomaly: a ridge at upper levels over SEA (see Parker et al., 2014 for a detailed analysis of this event). The downstream edge of the ridge was located over SEA with the potential for quasi-geostrophic forced subsidence. On 2 February, a new ridge formed started forming over eastern/southern Australia (Fig. 8e). On 5 February, yet another ridge formed over SEA (Fig. 8d) and remained stationary until the end of the heatwave on 9 February (Fig. 7c) as part of Rossby wave packet (P3 in Fig 6b) and reached over SEA on 5 February (Fig. 7d). However, the upper-level ridge was transient and was replaced by another ridge around 7 February as part of another amplified wave (P4 in Fig. 6, Fig. 7e).

No blocks were identified directly over SEA during the heatwave (Fig. 6, 7, 8). However, blocks were present throughout the heatwave frequent upstream of SEA from 50° E to 70° E in the Indian Ocean (B2 in Fig. 7b, 8b, Fig. 7), and downstream of SEA from 200° E to 250° E (B1 in Fig. 7b, 8). Three of the RWTs passing over Australia (T1, T2, T3 in Fig. 7b) seem to have formed downstream of the blocks in the Indian Ocean (Fig. 7b). Multiple Rossby wave breaking events were also associated with the RWTs during this (Fig. 6b, 7). Block B2 over the Indian ocean was particularly persistent and interacted with several amplified Rossby wave packets (T2, T4). B2 began to weaken around 2 February (Fig. 7c) but restrengthened again on 5 February (Fig. 8d) due to injection of low PV from a smaller southward moving block in the Indian Ocean (not shown). Therefore, B2 remained persistent throughout the heatwave. Rossby wave packet P1 formed downstream of the block B1 over the Pacific Ocean prior to the heatwave (Fig 6b, 7a).





400 Figure 7 So far, we have investigated the association of RRWPs with duration of hot spells. We also presented two cases of extreme and persistent SEA heatwaves to show how RRWPs can lead to the formation or replenish the anticyclonic PV anomalies over SEA. Figure B1 shows another case of SEA heatwave associated with RRWPs. In the next section, we extend the analysis to a climatological period (1979–2018) and explore high  $R_{SEA}$  conditions for all the SEA heatwaves.

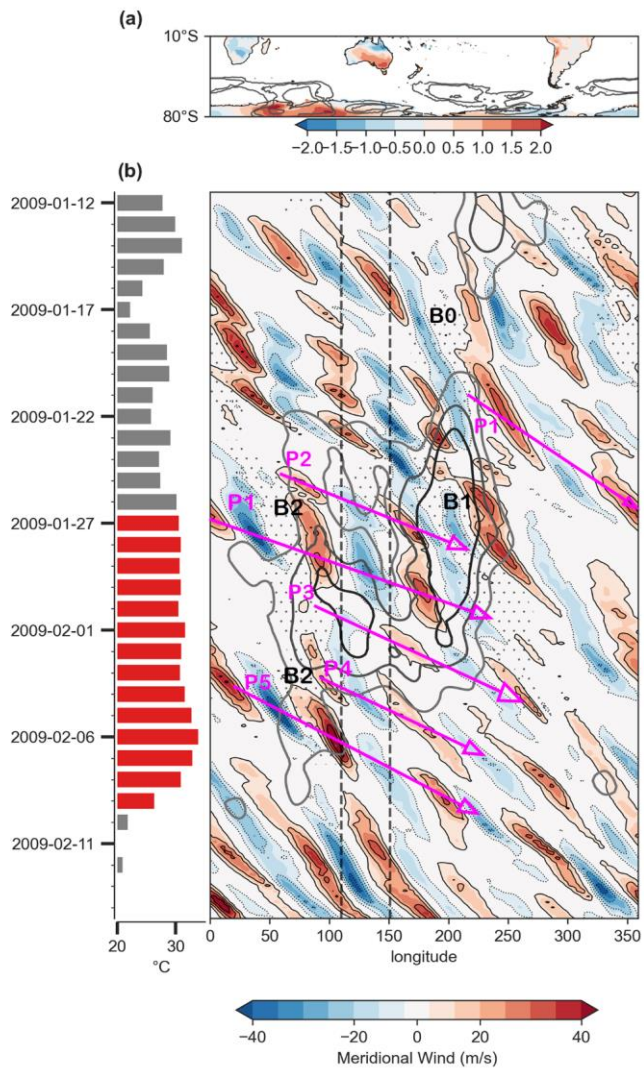
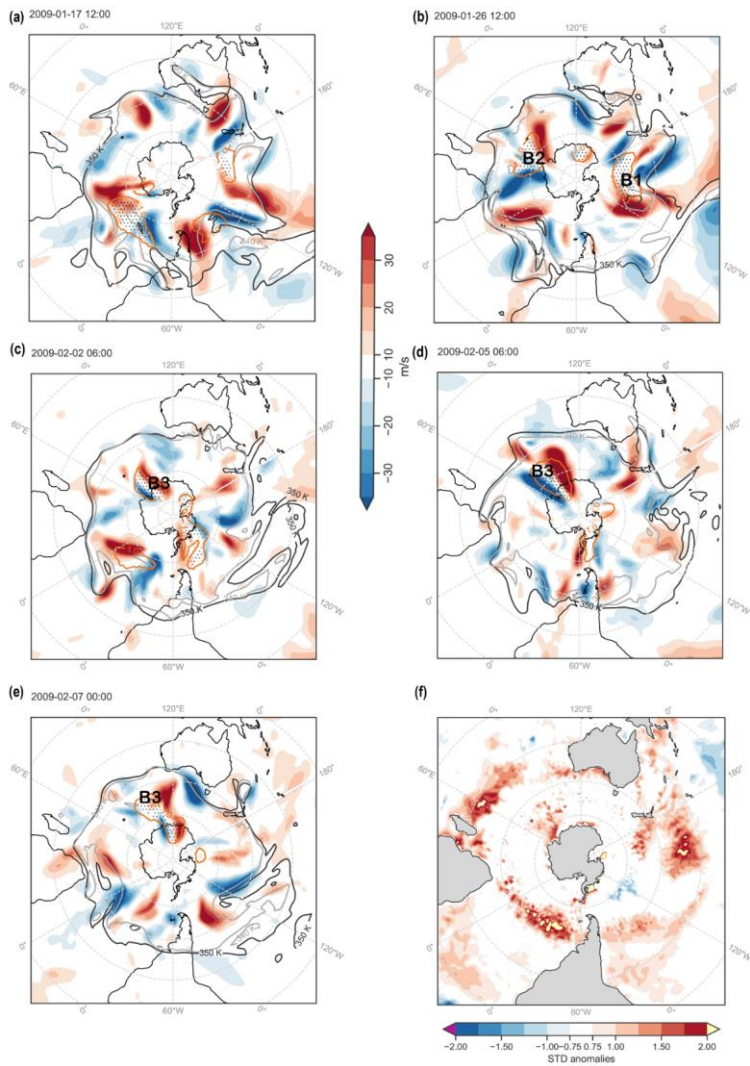
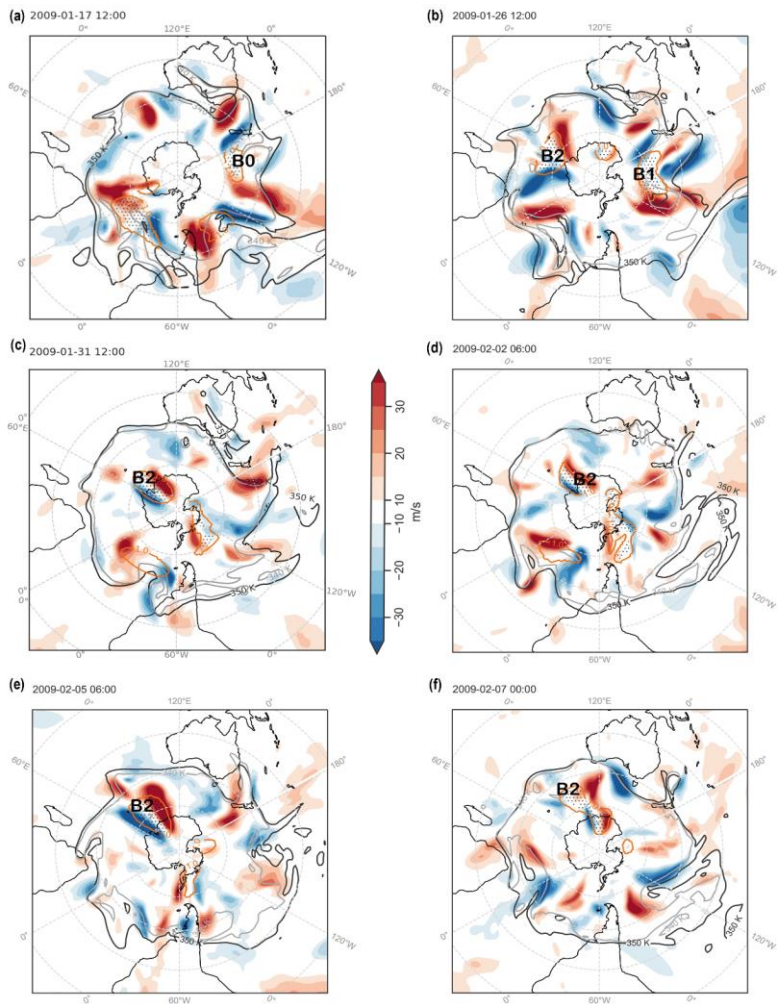


Figure 6: Same as in Fig. 54 but for February 2009 SEA heatwave.





405 Figure 87: Same as in Fig. 6 except for 2009 SEA heatwave.

period. In the next section, we assess the importance of RRWPs and QRA conditions for all the SEA heatwaves in the period 1979–2018 and establish whether they increase the probability of heatwaves or not.

### 3.3 Are RRWP conditions during SEA heatwaves more likely to occur with RRWPs or QRA?

|                          |                          | High $R_{SEA}$ | QRA-all    | QRA ( $k=4$ ) | QRA ( $k=5$ ) |
|--------------------------|--------------------------|----------------|------------|---------------|---------------|
| SEA heatwave days        | 461                      | 93             | 128        | 85            | 51            |
| SEA nonheatwave days     | 3059                     | 435            | 691        | 491           | 154           |
| <b>Total</b>             | <b>3520</b>              | <b>528</b>     | <b>819</b> | <b>576</b>    | <b>205</b>    |
| P(heatwave   R or QRA) % | $P_{\text{heatwave}}=13$ | 17.6           | 15.6       | 14.8          | 24.9          |

410 Table 1: Occurrence of High R and QRA on SEA heatwave days and the associated conditional probabilities of a heatwave given high R or a QRA day; QRA-all considers wavenumbers 4 to 6.

QRA with  $k=5$  has the highest conditional probability of heatwave: 25%, implying that out of 205 days with QRA conditions, 51 are heatwave days ( $51/205 = 0.25$ ). Both High  $R_{SEA}$  and QRA, including all wavenumbers, have conditional probability of heatwave greater than the reference climatology (Table 1). Heatwaves are 1.35 times more likely during high  $R_{SEA}$  days and 2 times more likely during QRA days with  $k=5$ . Parker et al. (2014a) assessed the conditional probability of heatwave over the state of Victoria for various large scale drivers. They found the highest conditional probability of Victorian heatwaves (12%) for Madden-Julian oscillation (MJO) phase 4. However, our results are not directly comparable to Parker et al.'s (2014a), because we define heatwaves over a larger region targeting SEA and use a slightly different heatwave definition. Given the importance of RRWPs and QRA over SEA, we next show their co-occurrence on a climatological timescale and diagnose their association with each other and with atmospheric blocks.

### 3.4 RRWPs, Atmospheric Blocking, and QRA

#### 3.4.1 Are RRWPs and QRA events independent?

The 2004 heatwave featured co-occurrence between RRWPs and QRA. This raises the question to what degree the two phenomena are exclusive or whether the metrics capture essentially the same flow structures but interpret them differently. Therefore, we examine the co-occurrence of high  $R$  events and QRA events on a climatological scale (December 1979–

February 2018). Because QRA is a hemispheric-scale metric, we consider a zonal mean  $R$  for a representation of hemisphere-wide recurrence. However, since RRWPs can occur locally, we performed sensitivity tests using zonal max  $R$  to define high  $R$  days. The zonal max approach did not change our conclusions.

|             | QRA  | No-QRA | Total |
|-------------|--|--------|-------|
| High $R$    | 25   | 11     | 36    |
| No high $R$ | 29   | 170    | 199   |
| Total       | 54   | 181    | 235   |
| Odds Ratio  | $\frac{25 \times 170}{29 \times 11} = 13.32$ |        |       |

**Table 2. Contingency table for high  $R$  and QRA events in DJF. Note that the table only includes independent events.**

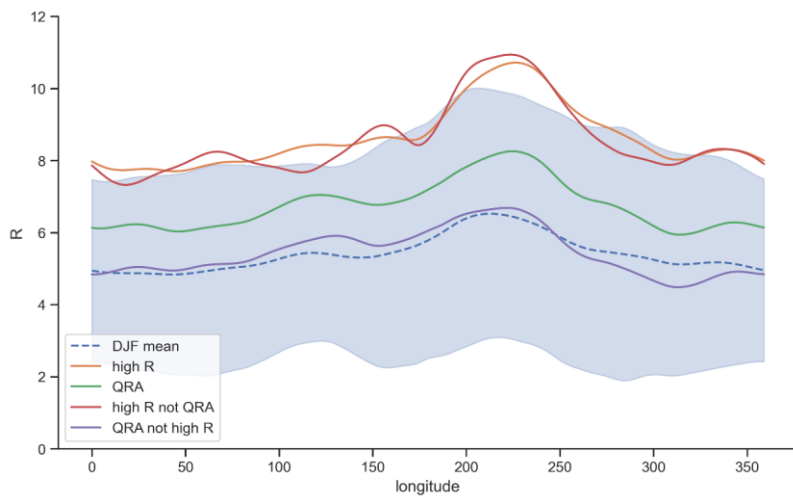
430 We find that 331 of 528 high  $R$  days (63%) correspond to QRA days. Conversely, 331 of 819 QRA days (40%) correspond to high  $R$  days. However, these two metrics are highly auto-correlated as they use 15 day running mean fields. Thus, to test the association between the two metrics, we use every 15<sup>th</sup> observation to have independent events. The co-occurrences of the two metrics are summarized in a contingency table (Table 2). We test the association between high  $R$  and QRA events using a chi-square test at 99% threshold, where the null hypothesis is: there is no association between high  $R$  and QRA events. The odds ratio is used to quantify the strength of association between QRA and high  $R$  events. The odds of a QRA event given high  $R$  is 25/11. The odds of a QRA event given no high  $R$  is 29/170.

435 The odds ratio is thus  $\frac{25/11}{29/170} = 13.32$ .

Thus, QRA has higher odds of occurring with high  $R$  events than without high  $R$  events. The chi-square test also shows a significant association between the two, suggesting that the null hypothesis that there is no association between high  $R$  and QRA events can be rejected. We find that our test results are robust with respect to the starting step of the 15 day intervals.

440 In figure 9, we compare the zonal spread of mean  $R$  values for different samples: high  $R$  (528 days), QRA (819 days), high  $R$  but not QRA (197 days), and QRA but not high  $R$  (488 days). Highest recurrence is seen over the south Pacific Ocean for all the samples. The sample belonging to high  $R$  but not QRA days shows the highest mean values probably due to the smallest sample size. QRA days show higher mean  $R$  than DJF mean as 40% of QRA days are comprised of high  $R$  days. Removing the high  $R$  days from the QRA sample drops the mean  $R$  values making it indistinguishable from the DJF mean.

The frequency analysis indicates a reasonably strong association between high  $R$  and QRA conditions but does not alone offer any meteorological interpretation. Therefore, we calculate composites of tropopause level potential vorticity (PV) and zonal winds for high  $R$  and QRA days (Fig. 10).



450 **Figure 9:** A comparison of mean  $R$  values for different samples shown in legend. Shading shows  $R$  values within one standard deviation for DJF.

### 3.4.2 How similar or different are upper-level flow conditions during RRWPs vs QRA days?

The anomaly structures for PV at 350 K and zonal wind at 250 hPa (U250) show a remarkable similarity between high  $R$  and QRA condition days: a Pearson correlation coefficient of almost 1 between high  $R$  days and QRA days for composite mean PV and composite mean U250 fields, respectively. Anomalies of PV composites with respect to the DJF climatology for both QRA and high  $R$  days (Fig. 10a, 10b) feature cyclonic PV anomalies north of New Zealand, in the Pacific Ocean, and upstream of South America. Similarly, anticyclonic PV anomalies are present in all the major ocean basins, including downstream of Australia, upstream of South America, and both upstream and downstream of South Africa. Increase in blocking frequency (crossed hatches in Fig 10a, 10b) is also seen mainly over south Pacific Ocean. Similarly, spatial features of the U250 anomalies (Fig. 10d, 10e) show a striking similarity between the two composites, with stronger westerlies over

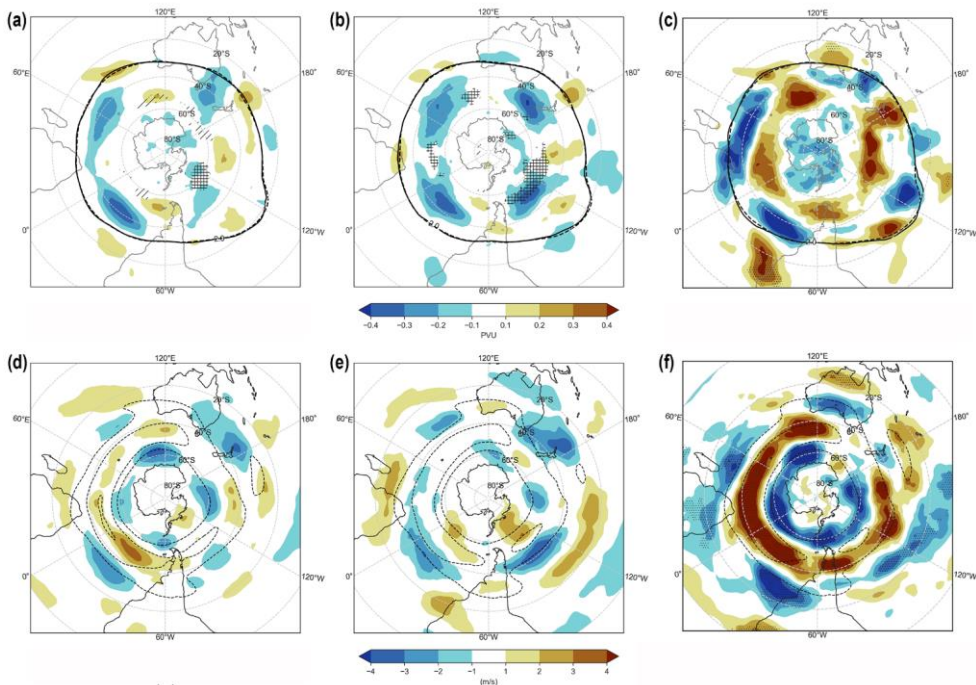
455

460

the South Atlantic Ocean and weaker zonal winds over SEA. However, a key difference is visible upstream of South America, where high  $R$  days show positive U250 anomalies north and south of the climatological jet core and negative U250 anomalies at the climatological jet core, thus favouring a meandering jet. The major features in the spatial distribution of anomalies for high  $R$  days are robust when testing the sensitivity by defining high  $R$  days with zonal maximum  $R$  values instead of the zonal mean  $R$  values used here. This suggests that the basin-wide high  $R$  values projects out in the zonal mean fields as well.

Subsequently, we compare the sample of QRA days exclusive of high  $R$  days with those of high  $R$  exclusive of QRA days for PV and U250 fields respectively. The null hypothesis tested is that the two samples belong to the same distribution. A two sample Kolmogorov–Smirnov ( $K-S$ ) test at 5% threshold is used to evaluate the null hypothesis with maximum FDR at 10%. The resulting significant area, where null hypothesis is rejected, is shown with dotted hatches (Fig. 10e, 10f). Significant areas difference in composite mean PV fields between the two samples include cyclonic PV anomalies over parts of Brazil, central Australia, and Pacific Ocean. The difference in composite mean U250 fields suggests strengthening of the westerlies and narrowing of the climatological jet (dotted isolines in Fig. 10f) over all the three ocean basins for QRA days exclusive of high  $R$  days compared to high  $R$  days exclusive of QRA.





475 **Figure 10: Anomalies of composite mean field with respect to DJF climatology for QRA (left), high R (middle). Right column show the difference of mean fields between QRA but non-high R days and high R but non-QRA days (right). (a), (b), and (c) show PV anomalies at 350 K isentropes. (d), (e), and (f) show zonal wind (U) anomalies at 250 hPa (m/s). Dashed contours in (d), (e) show isolines of mean U at 20, 30, 40 m/s. (f) show DJF mean U isolines. The solid contour in (a), (b) shows mean 2PVU at 350 K isoline for the respective variable and in (e) shows the same for QRA but non-high R days. The dashed contours in (a), (b), (c) show the 2PVU at 350 K contour for DJF mean climatology. Crossed (lined) hatches in (a), (b) show areas where blocking frequency anomalies (%) with respect to DJF climatology is greater (less) than 2%. Dotted hatches in (e) and (f) show significant regions tested using K-S test at 5% threshold.**

### 3.4.3 Does blocking area increase during high R or QRA conditions?

485 To analyse whether high R or QRA conditions increase the area of the blocks, we compare the blocks between 40° S and 70° S. First, the blocking area for each unique block is extracted at the time of maximum amplitude of PV and characterized with respect to high R or non-high R and QRA or non-QRA conditions. The resulting kernel density estimation functions are

shown in Fig. 11a. The sample size for each category in the same order is 86, 445, 101, and 421. For the 101 blocks with QRA days, 68 and 33 samples belong to QRA with wavenumber 4 (k4) and QRA with wavenumber 5 (k5), respectively.

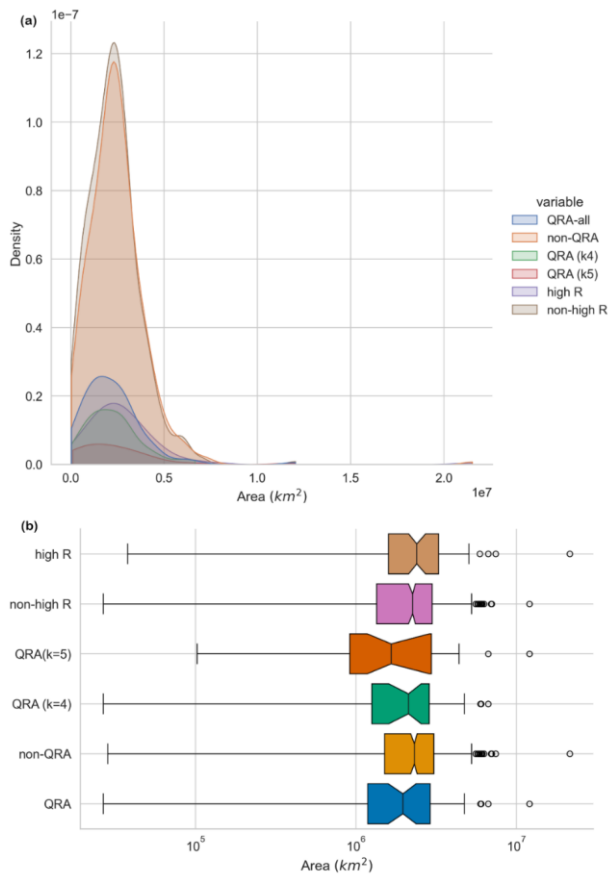


Figure 11: A comparison of area ( $\text{km}^2$ ) of atmospheric blocks for various categories. (a) Kernel density estimation (KDE) of the blocking area. (b) box plot of blocking area for the categories shown in the legend.

Density curves for the blocking area show a unimodal distribution for all the categories, with slightly right-skewed curves in most of the cases. Box plots of the blocking area under high  $R$  days show a marginally higher median than non-high  $R$  days whereas the blocking area under QRA days shows a marginal decrease in median compared to blocks with non-QRA days. Whether the medians in these categories are significantly different or not is evaluated using a Mann–Whitney U test, a non-parametric test which does not require the samples to be normally distributed, using a two-sided hypothesis at 5% significance level. We did not find a significant difference in the median area of blocks for either the case of high  $R$  vs non-high  $R$  or QRA vs non-QRA days (Fig. 11b).

#### 3.4.4 How are blocks spatially distributed for high $R$ and QRA days?

Mean blocking frequency for high  $R$  days (Fig. 12c) shows a statistically significant increase in blocking frequency in DJF mainly over parts of two ocean basins: upstream of South America in the Pacific Ocean, and upstream of Australia in the Indian Ocean. These are also the regions where blocking frequency is highest in the DJF climatology (Fig. 12a). Other areas with a significant increase include part of the Antarctic Sea (180°W), south of Africa, whereas a significant decrease is observed over parts of Antarctica. The significance was assessed using Mann–Whitney U test, which assesses the null hypothesis that distribution of blocks under high  $R$  (QRA) days and that of DJF climatology are equal. For QRA days (Fig. 12b), there is a significant decrease in blocking frequency over south of Australia and New Zealand, south of Africa, and over parts of the south Atlantic Ocean, which was not seen for high  $R$  days. In contrast, the region upstream of South America shows an increase similar to high  $R$  days. Although most of the grid points for QRA days (Fig. 12b) are not statistically significant, the overall decrease in blocking frequency is consistent with the results in Fig. 11b, which show a slight decrease in the median blocking area for QRA days.

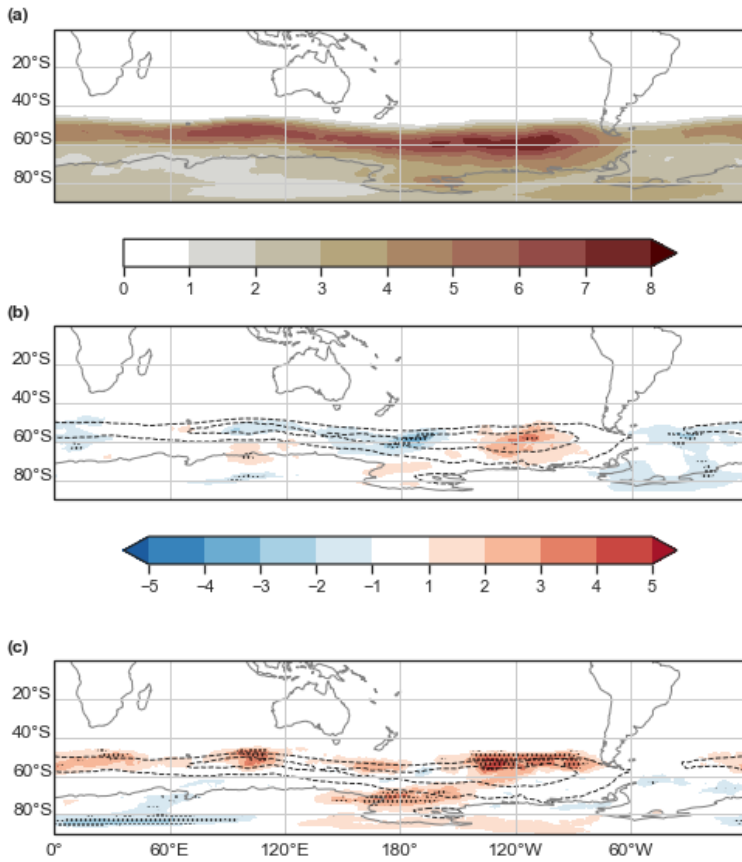


Figure 12: Blocking frequency (%) for (a) DJF, (b) difference between the mean blocking frequency (%) for QRA days and the DJF mean frequency, and (c) difference between the mean blocking frequency (%) for days with high-R days present and the DJF mean frequency. Dashed lines in (b) and (c) show DJF mean blocking frequency contours drawn at 4, 6, and 8%. Dotted hatches in (b) and (c) show grid points with statistically significant difference in the composite mean to the mean of the sample in (a) assessed using a Mann-Whitney U test with FDR at 5%.

515

520 First, a note on the co-occurrence of high  $R_{SEA}$  days and SEA heatwave days (SEA HD) as defined in section 2.3. Out of 352 days with high  $R_{SEA}$ , 67 co-occur with SEA HD and 285 do not co-occur (Table C1). Thus, the conditional probability of a SEA HD given high  $R_{SEA}$  is 0.19 ( $67/352=0.19$ ), which is higher than the climatology ( $457/3520=0.13$ ). Many high  $R_{SEA}$  days do not co-occur with SEA HD, which clearly indicates that  $R$  is not a sufficient condition for SEA heatwaves on its own.

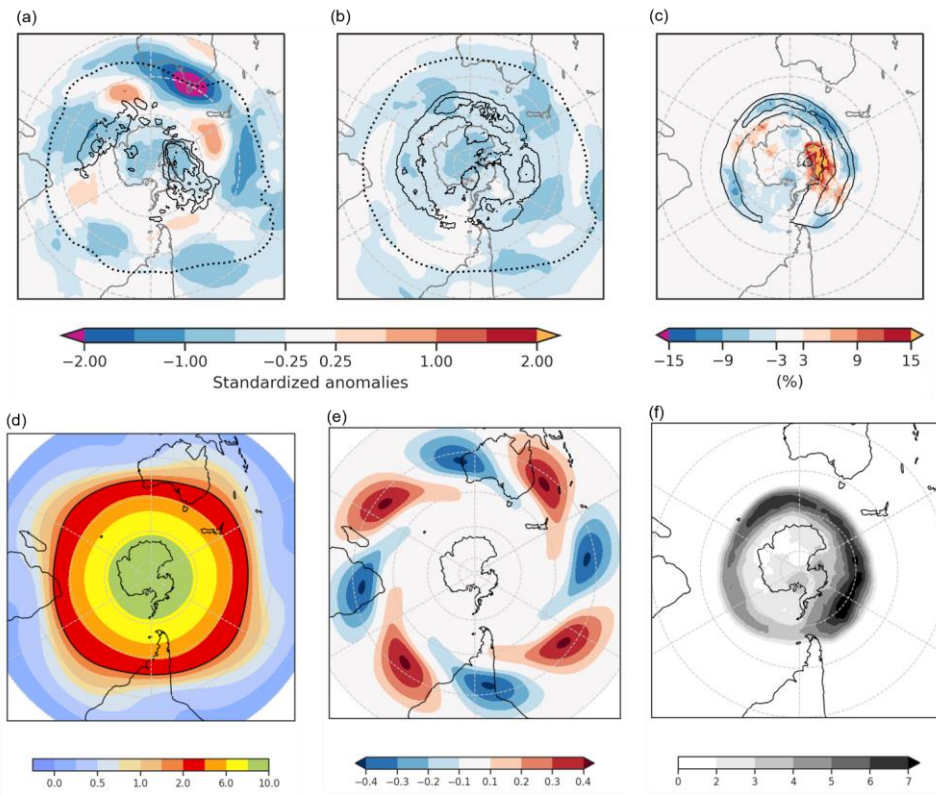
525 We, therefore, further explore that why some high  $R_{SEA}$  days co-occur with SEA HD while others do not.

High  $R_{SEA}$  days co-occurring with SEA HD feature a large anticyclonic PV anomaly over SEA (Fig. 8a) on the 350 K isentropic surface. The 2 PVU isoline on the 350 K isentropic surface, indicating the dynamic tropopause, is also located over SEA, thereby indicating a suitable choice of the isentropic surface. Upstream and downstream of the anticyclonic PV anomaly over SEA feature cyclonic PV anomalies that are also located equatorward of the highest blocking frequencies

530 (black contours in Fig. 8a). These may correspond to the cyclonic PV anomalies surrounding omega-type blocking or the cyclonic PV anomalies of the dipole blocks. Since blocking is a binary dataset, the blocking frequency in Figures 8a and 8b indicates the percentage of days on which a grid point features a block. Thus, for high  $R_{SEA}$  days co-occurring with SEA HD, blocks are more frequent over the Indian and the south Pacific Oceans close to the Antarctic coast compared to high  $R_{SEA}$  days without co-occurring SEA HD (Fig. 8a, 8c) and less frequent over the 60° S latitude, the latitudinal band featuring high

535 blocking frequency in the DJF climatology (Fig. 8c, 8f). In contrast, on high  $R_{SEA}$  days not co-occurring with SEA HD there is no spatial preference for the anticyclonic PV anomalies. Weak zonally elongated PV anomalies are present over the ocean basins, that are co-located with the blocking frequency fields (black contours in Fig. 8b). Near Australia, the centroid of the contour of anticyclonic PV anomaly appears around 30° downstream of SEA over New Zealand (Fig. 8b) compared to over SEA in Figure 8a. The difference in the spatial distribution of PV anomalies on the high  $R_{SEA}$  days not co-occurring with

540 SEA HD and the high  $R_{SEA}$  days co-occurring on SEA HD suggests that only the RRWPs whose phase is conducive to forming ridges over SEA are important for SEA heatwaves.



545 **Figure 8: Standardized PV anomalies on the 350 K isentropic with respect to the DJF climatology (1979–2018) for (a) High  $R_{SEA}$  days and SEA heatwave days (HD), (b) High  $R_{SEA}$  days and non-SEA HD. Dotted black lines show 2 PVU contour in the mean PV fields for (a) and (b), and black contours show mean blocking frequency contours at 5, 10, 15 % for the same. (c) Shows the difference in blocking frequency between (a) and (b), and black contours show the same at 4, 6%. (d) Shows the sum of PV (in PVU) from the zonal wavenumber,  $k = 4$  component of the DJF climatology at 350 K (shown in e) and the  $k=0$  (the DC) component. (f) Shows the climatological mean blocking frequency (%) for DJF, and black contours in (c) show the same at 4, 6%.**

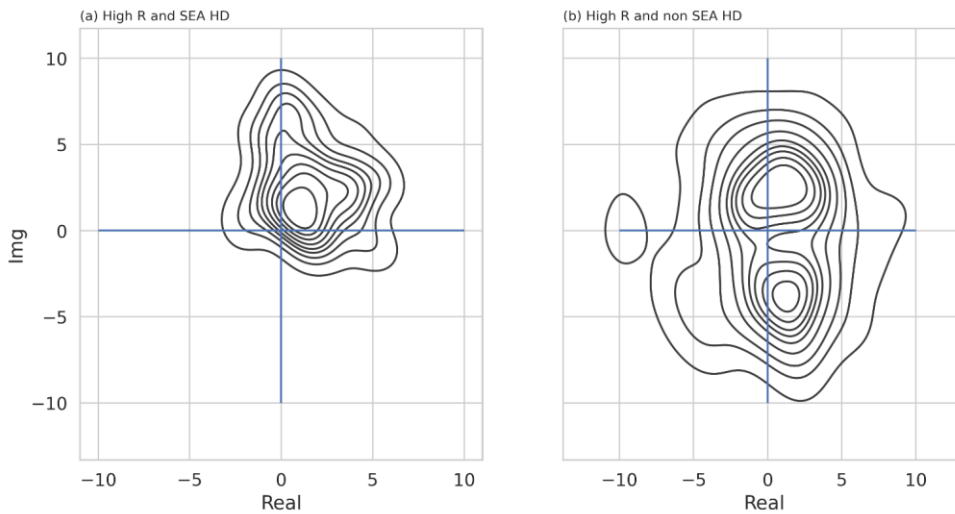


**Figure 9. Bivariate kernel density estimate using Gaussian kernels in the complex plain of the Fourier decomposed meridional wind at 250 hPa averaged between 35°S and 65°S. Only zonal wavenumber 4 is shown for days belonging to (a) high  $R_{SEA}$  and SEA HD, and (b) high  $R_{SEA}$  and non-SEA HD.**

In addition to the ridge over SEA, a circum-hemispheric zonal wavenumber 4 (WN4) pattern is present in the composite mean PV fields for high  $R_{SEA}$  days co-occurring on SEA HD (Fig. 8a). This WN4 pattern does not have the same distribution of PV anomalies as the WN4 extracted from the Fourier decomposition of the climatological mean PV field for DJF: the WN4 climatology features the anticyclonic PV anomaly node roughly 30° west of SEA (Fig 8d, 8e).

A high fraction of WN4 flow during high  $R_{SEA}$  days co-occurring on SEA HD is in phase (Fig. 9). Figure 9 shows the phase and amplitude density distribution of the WN4 component of the meridional winds averaged between 35° S and 65° S. Phase and amplitude information for each wavenumber can be extracted using a Fourier decomposition as shown in section 2.1. On high  $R$  and SEA HD, the density distribution in the complex plain is unimodal point to a preferred phasing of the wave that is reflected in WN4 pattern visible in the PV composite (Fig. 8a). On high  $R_{SEA}$  and SEA HD density distribution in the complex plain is bimodal and generally much broader, that agrees with the PV composite that shows no clear WN4 pattern (Fig. 8b). The phase distribution for wavenumber 4 is shown here because it emerges as the dominant pattern in the

565 composite mean (Fig. 8a), whereas density distributions for other wavenumbers do not exhibit a clear difference (not shown). Overall, our results agree with the understanding of SEA heatwaves featuring upper-level anticyclonic PV anomalies over SEA (Marshall et al., 2013; Parker et al., 2014b; Quinting and Reeder, 2017), and we show how RRWPs in a particular phase are conducive to forming anticyclones over SEA.

#### 4. Discussion

570 We first summarize key criteria used in the objective identification of the weather features, blocks and RRWPs, and the QRA mechanism. The defining spatial and temporal characteristics of blocks, QRA, and RRWPs used in their automatic detection algorithms are summarized in Table 1. The zonal spatial scale of the structures increases from regional to basin-wide for blocking, through regional, basin-wide to semi-hemispheric for RRWPs, to hemispheric for QRA.

| Characteristics           | Blocks<br>using Schwierz et al.'s (2004)<br>algorithm | RRWPs using Rothlisberger<br>et al.'s (2019) algorithm | QRA using Kornhuber et al.'s<br>(2017b) algorithm                           |
|---------------------------|---|--|---|
| Input variable            | PV (vertically averaged<br>between 500–150 hPa)       | Wavenumber filtered V at 250<br>hPa                    | Zonal mean U at 300 hPa for<br>waveguide, Thermal and<br>Orographic forcing |
| Presence of<br>waveguide  | No  | No   | Yes   |
| Wavenumber<br>filtering   | No wavenumber filtering                               | $k = 4–15$   | Focus on $k \geq 4$   |
| Persistence/<br>timescale | Minimum persistence of 5<br>days                      | 14 day running mean fields                             | 15 day running mean fields  |
| Spatial scale             | Regional to basin-wide                                | Regional, basin-wide, or semi-<br>hemispheric          | Hemispheric   |



**Table 3: A comparison of the criteria used to automatically identify blocking, QRA, and RRWPs.**

575 RRWPs can be regional, basin-wide, or semi-hemispheric in spatial extent. Yet, a zonal-mean approach finds that 40% of high- $R$  days coincide with QRA days. This is partly because a regionally amplified pattern can influence zonal-mean fields. For example, we found a high correlation between the high- $R$  days defined with zonal means with the high- $R$  days defined with zonal-maximum- $R$  fields. Moreover, a recurrent transient wave pattern can appear as a quasi-stationary signal when averaged over time. Furthermore, amplified Rossby waves may influence the metrics used here for objectively detecting blocking, RRWPs, and QRA. For example, the amplified Rossby waves during the 2004 SEA heatwave (Fig. 5), aided by recurrence, resulted in high- $R$  values, corresponded regionally to blocking, and were identified as a QRA event. These amplified waves were clearly composed of recurring transient waves with nonzero phase velocity (Fig. 5).

580 The link between high- $R$  and QRA events is not only reflected in high co-occurrence but also in spatial patterns. The upper-level-mean-PV composites for QRA and high- $R$  days show a remarkably similar pattern (Fig. 10). The pattern is statistically indistinguishable even though the zonally averaged- $R$  metric does not explicitly include any phase or location restriction. This implies that high- $R$  events in the SH co-occurring with QRA have a particular phase preference. The PV anomaly pattern exhibits a wavenumber 4 structure in the extratropics and a wavenumber 5 to 6 pattern in the subtropics (Fig. 10).

585 Hence, the question is whether RRWPs and QRA may in some cases be the same structures observed through different lenses, i.e., with diagnostics from temporal, spatial, and other filters. The similarity in the composite PV anomalies during high- $R$  and QRA days point to the same mechanisms being relevant for the organization of the RRWPs, the establishment of QRA conditions, and/or interactions between the two.

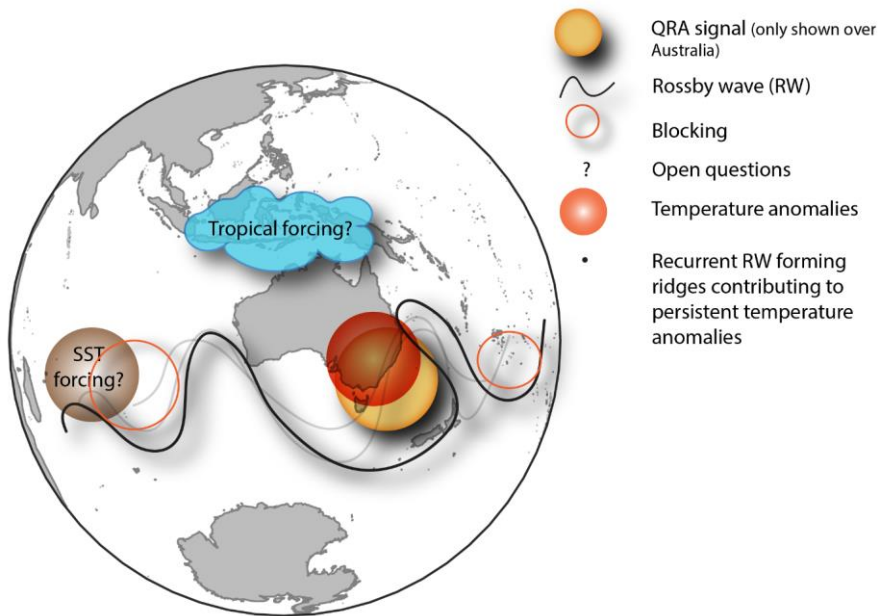
590 The fact that not all high- $R$  and QRA days overlap—37% (197 days) of high- $R$  days do not feature QRA conditions—may be explained by the different longitudinal scales used by the detection algorithms. Another reason could be the forcing condition required for QRA events; not all high-amplitude waves are detected by QRA because QRA needs the presence of a waveguide as well as thermal and orographic forcing (Petoukhov et al., 2013; Kornhuber et al., 2017b). Moreover, the composite PV for QRA days exclusive high- $R$  days showed significant differences to high- $R$  days exclusive of QRA over several key regions: parts of Brazil, central Australia, and the south Pacific Ocean (Fig. 10c).

595 The schematic in Fig. 12 illustrates hypotheses of interactions between RRWPs, QRA, and blocking during SEA heatwaves. Direct interactions between RRWPs and QRA conditions might include momentum fluxes associated with Rossby wave

600 breaking that may establish background flow conditions conducive to QRA. External mechanisms of importance might be planetary-scale stationary waves of the extratropical flow that organize synoptic-scale Rossby waves, and hence RRWPs, and that may contribute to QRA conditions. These waves might be forced by sea surface temperature anomalies (e.g., O'Brien and Reeder, 2017) and tropical sources (e.g., Hoskins and Sardeshmukh, 1986). Tropical forcing in the form of enhanced convection due to an active MJO was present during the 2009 heatwave (Parker et al., 2014b), for which RRWPs were also observed (Fig. 5).

605 Climatological interactions between blocks and RRWPs take the form of significant increases in blocking frequency over parts of south Pacific and Indian Ocean. Increased  $R$  anomalies are seen upstream and downstream of blocks in the south Pacific Ocean (Fig. C1), similar to the relationship shown in the Northern Hemisphere basins (Röthlisberger et al. 2019). During SEA heatwaves, blocks were not detected directly over SEA in either of the cases that we analysed, even though anticyclonic PV anomalies are a common feature of SEA heatwaves (Parker et al., 2014b, see also Fig. 6, 8). The climatological blocking frequency (Fig. 12a) clearly indicates that the blocking metric primarily detects blocking further poleward. Sensitivity tests with a slightly different setting (threshold of 1.0 PVU), which should capture blocks further equatorward (Pfahl and Wernli, 2012), did not detect the subtropical ridges over SEA in either of the two case studies. Moreover, the ridges over SEA were relatively transient during the 2004 and 2009 heatwaves. However, these ridges are 615 extremely important to identify; thus, developing algorithms to identify subtropical ridges over SEA would be beneficial (Sousa et al., 2021).

620 However, blocks frequently featured upstream of Australia during the two heatwaves and played a role in initiating Rossby waves and organizing their phases, resulting in RRWPs. Blocks were also significantly frequent in parts of Pacific and Indian Oceans for days featuring RRWPs. The recurrent upper-level ridges associated with the RRWPs played a role in reinforcing surface weather. QRA with  $k=5$  was observed simultaneously with RRWPs during the 2004 heatwave. Both the cases also showed high nonlinearity in the flow as breaking Rossby waves. The PV anomalies from the resulting wave breaking played a vital role in amplifying upstream blocks (e.g., Shuts 1983, Pelly and Hoskins 2003) and triggering Rossby waves (e.g., Martius et al., 2010, Röthlisberger et al., 2019).



625 **Figure 13: Postulated schematic of interaction between atmospheric blocks, RRWPs, and QRA.**

During the 2004 and 2009 SEA heatwaves, we find transient and fast-moving Rossby waves organized in wave packets, recurring in the same phase to form a ridge over SEA, thereby contributing to the persistence of the heatwave conditions. This persistence arises by recurrence, in contrast to the persistence arising from stationary weather features such as slow-moving Rossby waves (e.g., Wolf et al., 2018) or blocking anticyclones (e.g., Kautz et al. 2022). The Rossby wave packets observed during the two SEA heatwaves were not always initiated in the same area. In the 2004 case, these waves were mostly not in phase upstream of Australia, whereas in the 2009 case, they were also in phase upstream over the Indian Ocean. Blocks were observed upstream and downstream during the two heatwaves and suggests that blocks could play a role in initiating the RWPs and/or in modulating their phase. Figure D1 presents relationship between  $R$  anomalies and the blocks in the Indian and south Pacific Oceans for DJF. Overall, our results agree with Risbey et al. (2018) and King and Reeder (2021), who reported transient waves in the Indian Ocean preceding SEA heatwaves and transient circulation anomalies

635

during SEA heatwaves. More specifically, we show how recurrent Rossby waves aid in the persistence of the well-known upper-level anticyclonic PV anomalies during SEA heatwaves by forming recurrent upper-level ridges.

The relevance of RRWPs for persistent SEA heatwaves documented in these two case studies is consistent with the results of the Weibull regression analysis, which reveals a significant positive statistical link between the duration of hot spells over

640 SEA and RRWPs. PV composite for high  $R_{SEA}$  days co-occurring with SEA heatwaves shows an anticyclonic PV anomaly over SEA (Fig. 8), which is a typical feature of SEA heatwaves (Parker et al., 2014b; Quinting and Reeder, 2017). The PV composite also shows a wavenumber 4 pattern, where the anticyclonic PV anomalies are located upstream and downstream of blocking frequency maxima. Furthermore, the distribution of the zonal wavenumber in the complex plain indicates a preferred phasing for high  $R_{SEA}$  days part of SEA heatwaves (Fig. 9). The results from the Weibull regression analysis also

645 suggests preferred phasing of the transient eddies not only over SEA but also upstream and downstream of it. Therefore, recurrent Rossby wave packets in the right phase could help to foster the anticyclonic anomalies over SEA for time periods exceeding the lifespan of an individual wave packet. Hence, the combined evidence from the literature summarized above, together with the observations from the two case studies and the results from the regression analysis, suggest a causal link between RRWPs and persistent SEA heatwaves. The proposed link works as follows: heatwaves over SEA are forced by subsidence occurring in anticyclones of SEA (e.g., Quinting and Reeder, 2017). RRWPs result in the repeated formation of these ridges over SEA and thereby contribute to the persistence of the ridges and thus, the heatwaves. However, not all SEA HD are associated with RRWPs, and hence other dynamical pathways for SEA heatwaves exist. In addition, local negative soil moisture anomalies strengthen positive temperature anomalies through increased surface sensible heat fluxes and may thereby extend the duration of heat waves (e.g., Green 1977; Seneviratne et al. 2010; Martius et al. 2021).

655 A reverse causal link between surface temperature anomalies during SEA heatwaves and  $R_{SEA}$  is theoretically possible, namely that the positive surface temperature anomaly contributes substantially to the upper-level ridge and that this ridge amplification increases  $R_{SEA}$ . This causal link cannot be distinguished in our Weibull model set-up. However, model experiments from Martius et al. (2021) suggest that the influence of surface temperature anomalies over Australia on the upper-level (250hPa) geopotential height and wind anomalies is quite small; therefore, the imprint on R-metric after the

660 latitudinal averaging is even smaller.

## 5. Conclusions

To conclude, we answer the research questions put forward in this study.

Are RRWPs relevant for persistent hot spells in the SH and if so, in which regions? We saw find that RRWPs are associated with a significant increase in the duration/persistence of persistent hot spells significantly over in the SH. In several regions of the SH. Several parts of SEA, including the states of South Australia, New South Wales, Victoria, and Tasmania experience, longer hot spells during coincide with high amplitude RRWPs (Fig. 3). Other regions over land where RRWPs are statistically associated with hot spell duration include South America: southern Brazil, Bolivia, and parts of Argentina and Chile.

How do SH RRWPs relate to SEA heatwaves, and do QRA conditions and blocks play a role? We showed that both RRWPs and QRA increase the probability of SEA heatwaves (Table 1). Heatwaves are two times more likely during QRA with wavenumber 5 and 1.35 times more likely high  $R_{SEA}$  days than reference climatology. The two case studies of the SEA heatwaves of 2004 and 2009 showed have demonstrated, the role of RRWPs in building persistent ridges over during two cases of SEA (Fig. 5 heatwaves: the 2004, and Fig. 7) 2009 heatwaves. Both heatwaves featured RRWPs comprised of transient Rossby waves, which were not in phase upstream of Australia. QRA with wavenumber 5 was observed during the 2004 heatwave, possibly contributing to the highly amplified flow conditions (see Fig. B1 for coincidence during 2014 heatwaves). Upper-level PV based blocks regionally but not hemisphere wide. Blocks were not directly observed over SEA but, but the case studies suggest that blocks upstream and downstream played an important role in initiating the Rossby wave trains. Both QRA and high  $R$  days could serve as important indicators for SEA heatwaves because they show conditional probabilities of SEA heatwaves that are comparable with remote drivers such as MJO and El Nino (Parker et al. 2014a).

However, the multiple pathways for SEA heatwaves implies that no single metric or diagnostic tool can be perfect.

How do RRWPs conditions relate to QRA conditions in the SH? We found a strong and statistically significant association between RRWPs and QRA events (Table 2); QRA events are more likely to occur with RRWPs than without RRWPs. We also showed that 40% of QRA days also feature high  $R$  days, indicating RRWP conditions, which implies that QRA conditions can often feature RRWPs. We also found similar flow conditions in the composite mean upper level fields during QRA and high  $R$  days. However, 60% of QRA days do not feature high  $R$ . Significant differences in flow conditions for

Formatted: English (United Kingdom)

Formatted: English (United Kingdom)

Formatted: English (United Kingdom)

Formatted: English (United Kingdom)

Formatted: English (United Kingdom)

QRA days exclusive of high  $R$  days with high  $R$  days exclusive of QRA days show cyclonic PV over parts of Brazil, central Australia, and south Pacific Ocean, and increased westerlies over all the three ocean basins.

How do RRWPs and QRA conditions relate to blocks in the SH? We found an insignificant increase in the median area of blocks for high  $R$  vs non high  $R$  in the SH and a similar decrease for QRA days vs non QRA days (Fig. 11). We looked  
690 packets and modulating their phase. We further into how blocks are spatially distributed for high  $R$  and QRA days, respectively (Fig. 12). Important differences can be seen between the two in blocking frequency over the Indian Ocean, south of Australia and New Zealand, south of Africa, and in the south Atlantic Ocean, whereas both show an increase in blocking frequency over the south Pacific Ocean. investigated the co-occurrence of RRWPs during the most persistent and extreme SEA heatwaves using the R-metric.

695 Furthermore, we proposed a schematic of how RRWPs, QRA, and blocking could co-exist or interact (Fig. 13); however, the hypotheses need to be tested further. Amplified Rossby waves can influence the metrics used to diagnose these features, and thus, we detect high co-occurrences between high  $R$  and QRA conditions. However, interactions between RRWPs, QRA, and blocks may occur via momentum fluxes associated with amplified waves, amongst other pathways. There may be potential common drivers such as enhanced MJO and SST forcing. Rossby wave breaking was frequently observed during  
700 the two case studies, which may have initiated Rossby wave trains. These Rossby waves recurred in the same phase over Australia but were not in phase upstream. Possible unexplored factors which can modulate the phase of these waves include stationary planetary waves and blocks.

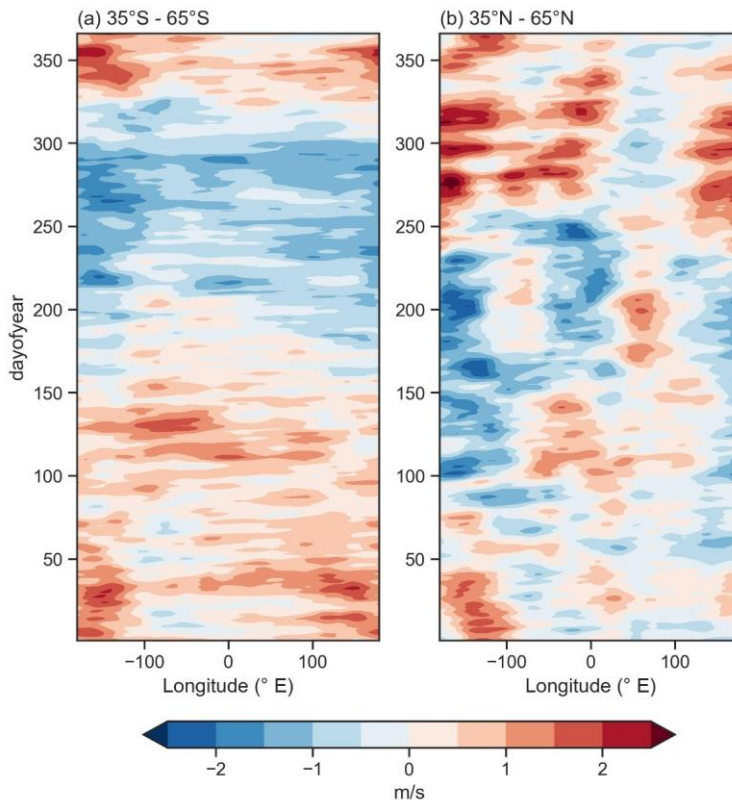
However, several questions that relate to the interaction between blocking, RRWPs and QRA remain open. Does blocking modulate the phase of Rossby waves and thus help in establishing RRWPs, or is the causal link instantaneous? What is the  
705 role of blocks during the QRA conditions, and why do we see a difference in blocking frequency between RRWPs and QRA conditions (Fig. 12)? The role of QRA in the recurrence of Rossby waves also needs to be investigated further. Investigating the role of background flow is not straightforward because defining it is a formidable problem (Wirth et al., 2018; see discussions in White et al., 2021). The interaction of RRWPs with other well-known climate oscillation patterns also needs to be investigated further. The improved understanding between the interplay of these features will help to reduce model  
710 biases and improve our confidence in future climate projections.

We find that days with  $R$  exceeding the 90<sup>th</sup> percentile, high  $R_{SEA}$  days, are associated with increased probabilities of being part of a heatwave compared to climatology. These conditional probabilities have similar magnitudes as those with remote drivers MJO, El Nino (Parker et al., 2014a). However, not all high  $R_{SEA}$  days are associated with heatwaves. Further investigations suggest that those high  $R_{SEA}$  days, that are relevant for the SEA heatwaves, play a role in forming or sustaining the ridges over SEA. Such high  $R_{SEA}$  days exhibit a circumglobal zonal wavenumber 4 pattern in the PV composite and indicate a preferred phasing of the waves. The high  $R_{SEA}$  days that do not coincide with SEA heatwave days do not show preferred phasing (a ridge or a trough) over SEA. Therefore,  $R$  accompanied with information on the phasing of the wave packets could be used as a diagnostic metric for SEA heatwaves.

The following open questions remain: what is the role of blocks in initiating RRWPs and modulating their phase? The case studies and the PV composites suggest that blocking might play an important role. What is the role of background flow in setting up RRWPs and modulating their phase? The interaction of RRWPs with other well-known climate oscillation patterns such as the El Nino-Southern Oscillation and the Southern Annular Mode also needs to be investigated further. Better understanding of the interplay between these features might offer an opportunity to improve sub-seasonal forecasts during RRWP events.

### Appendix A: Comparison of $R$ anomalies for Southern Hemisphere and Northern Hemisphere

Both the Southern and Northern Hemisphere  $R$  fields show seasonality. Anomalies are highest for Northern Hemisphere boreal autumn and winter days. Interestingly, the Southern Hemisphere shows higher  $R$  anomalies during austral summer days than winter days.

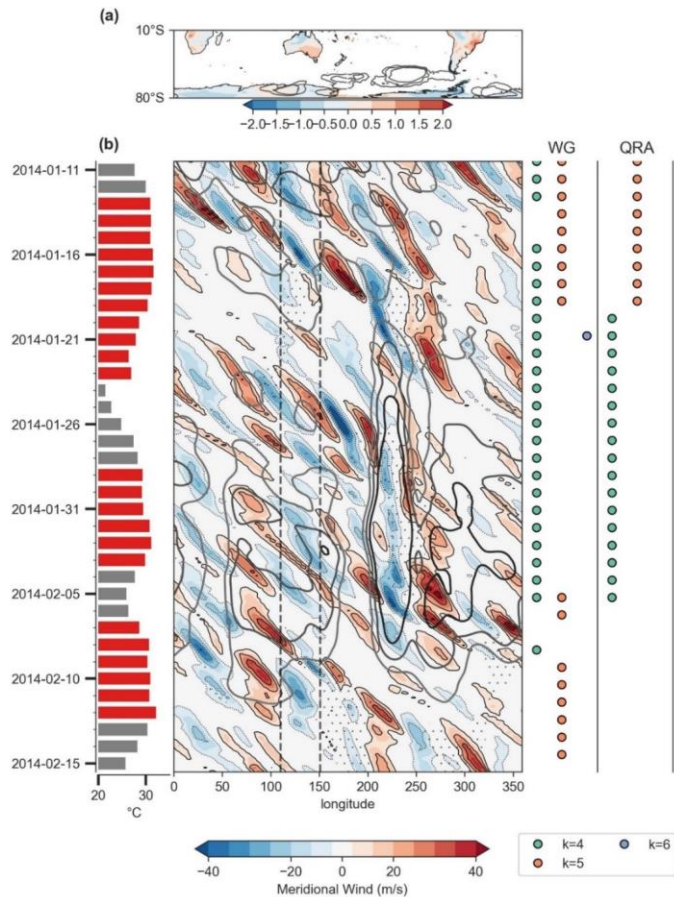


730

Figure A1:  $R$  anomalies for Southern and Northern hemispheres. Anomalies for day-of-year mean are calculated with respect to mean  $R$  fields.

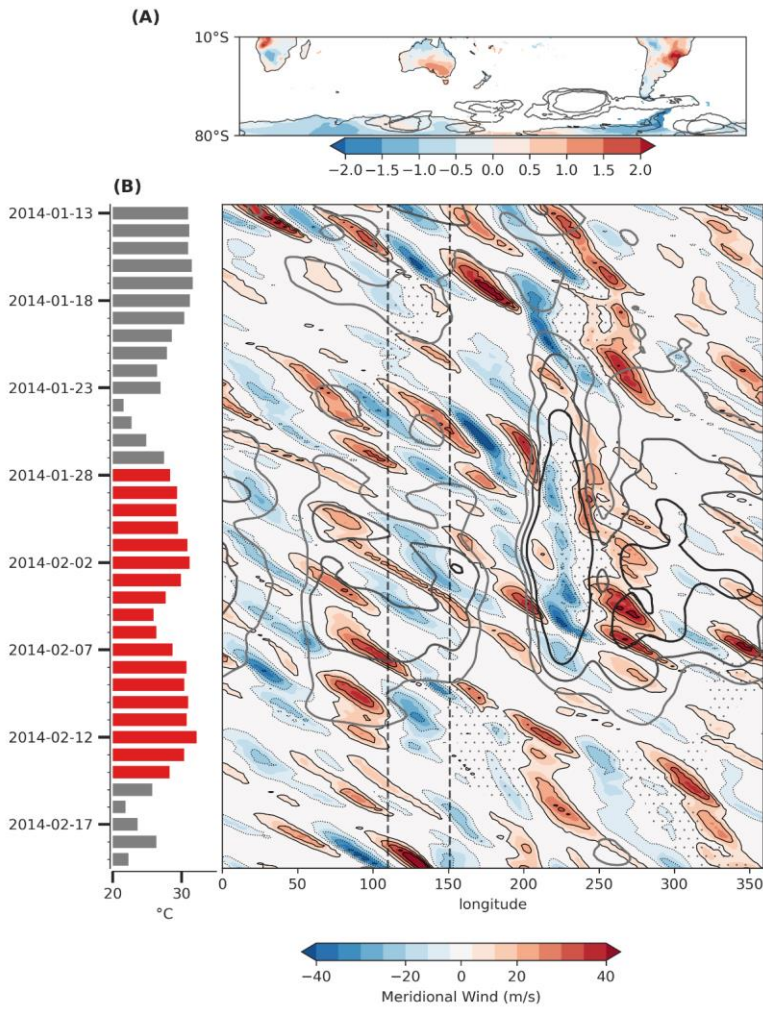


Appendix B: RRWPs and QRA during 2014 Heatwaves



735 **Figure B1: RRWPs, blocks, and QRA conditions during the 2014 SEA heatwave.** (a) Filled contours depict mean of standardized anomalies of daily maximum 2-m temperature over land from 2014-01-11 to 2014-02-14. Contours show mean blocking frequency during the heat wave (5, 10, 20%). (b) Bars show daily maximum 2-m temperature averaged over SEA (°C), and red marks the heatwave periods. The Hovmöller diagram shows the meridional wind at 250 hPa averaged between 35°S and 65°S (filled contours, m/s), R values (grey contours, 6, 8, 10 m/s), and longitudes at which at least one grid point between 30°S and 70°S featured an atmospheric block (stippling). The right columns in (b) indicate the presence of waveguides and quasi-resonance conditions with coloured dots indicating the respective wavenumber (see legend).

740



Appendix C:-

Figure B1: Same as in Fig. 4 but for January 2014 SEA heatwave.

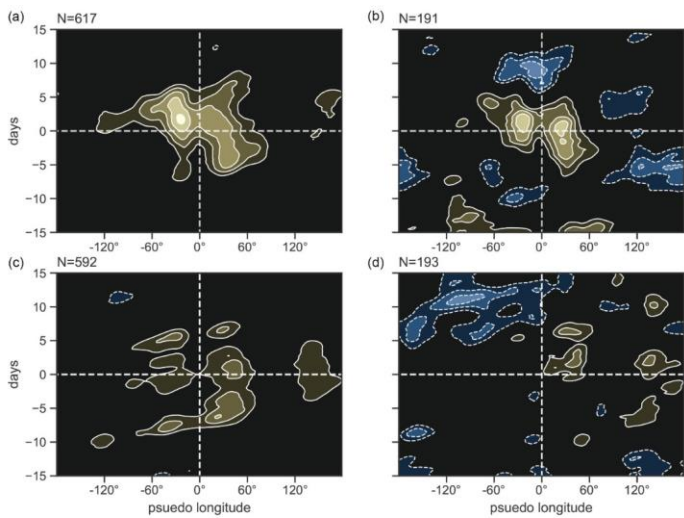
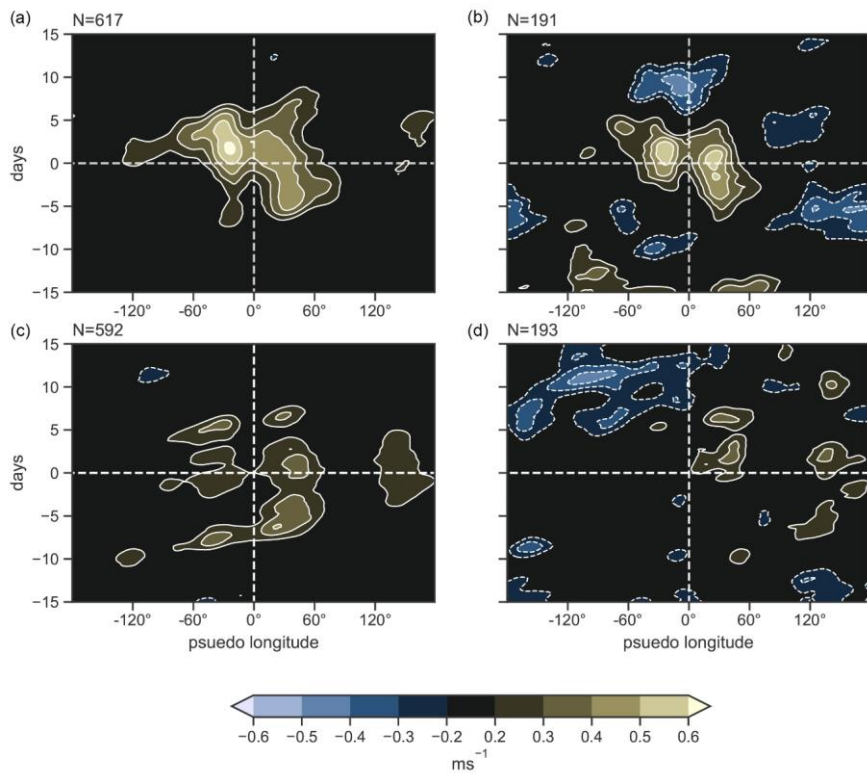
745 **Appendix C: Occurrence of High  $R_{SEA}$  on SEA heatwave days**

|                                   | <u>Days (DJF)</u>                              | <u>High <math>R_{SEA}</math> (days)</u>                            |
|-----------------------------------|--|--|
| <u>SEA heatwave days (SEA HD)</u> | <u>458</u>                                     | <u>67</u>  |
| <u>SEA non-heatwave days</u>      | <u>3062</u>                                    | <u>285</u>   |
| <b><u>Total</u></b>               | <b><u>3520</u></b>                             | <b><u>352</u></b>  |
| <u>Probability</u>                | <u><math>P_{\text{heatwave}} = 0.13</math></u> | <u><math>P(\text{SEA HD}   \text{High } R_{SEA}) = 0.19</math></u> |

**Table C1: Occurrence of High  $R_{SEA}$  on SEA heatwave days and the associated conditional probabilities of a heatwave given high  $R_{SEA}$ .**

**Appendix D: Relationship between blocks and RRWPs in the South Pacific and the Indian Ocean**

750



composites of  $R$  anomalies centred on the mean longitude and time of maximum amplitude of blocks located in Pacific Ocean (181–300° E, 30–80° S) in subplot (a) and (b), Indian Ocean (60–180° E, 30–80° S) in subplot (c) and (d). Left column includes blocks for all seasons and right shows for DJF.  $N$  denotes number of blocks for each category.

755 To further analyse the spatial distribution of RRWPs relative to blocks in the SH, we focus on two longitudinal subdomains that show a high blocking frequency in the DJF climatological mean (Fig. 11a): the South Pacific Ocean (230 – 310 °E), and the Indian Ocean (0 –90 ° E). We use time-lagged composite  $R$  anomalies with respect to the centroid of the blocks at the time of the maximum blocking amplitude in the two domains similar to Röthlisberger et al. (2019; see Fig. 12 in their paper). Here,  $R$  anomalies are calculated with respect to the day-of-year climatology.

760 In the Pacific Ocean, blocks coincide with positive  $R$  anomalies in a longitudinal band from ~60° upstream to ~60° downstream of the blocks (Fig. C1 a, b) from 5 to 8 days before the time of maximum blocking amplitude; this resembles a butterfly pattern, similar to blocks in the NH (Fig. 12, Röthlisberger et al., 2019). Similar to the NH,  $R$  anomalies in the Pacific Ocean are not high at the centroid of the block. This could be because the wavelength of the upper-level ridge associated with the block may be too wide to be captured by the  $R$  metric because the  $R$  metric only has contributions from  $k = 4$  and higher.  $R$  anomalies are consistent for DJF and blocks for all seasons in the Pacific. In contrast, in the Indian Ocean, seasonal variation is seen in  $R$  anomalies (Fig. C1 c, d), where blocks located in DJF show  $R$  anomalies downstream of the centroid of the block only and possibly show weak association with RRWPs.

#### Code and data availability

Code for calculating  $R$  metric is available on GitHub (Ali and Röthlisberger, 2021). ACORN-SAT data is available at <http://www.bom.gov.au/climate/data/acorn-sat/#tabs=ACORN%E2%80%90SAT>. QRA data can be requested from KK. The ERA-I reanalysis dataset used can be downloaded from <https://apps.ecmwf.int/datasets/data/interim-full-daily/levtype=pl/>.

#### Author Contributions

775 ~~OM, KK, MR, SMA conceptualized the study, and SMA and OM designed the methodology. SMA performed the formal analysis. TP provided heatwave data and contributed to heatwave analysis. KK provided QRA data. MR provided code for the Weibull regression model and guided SMA in applying it. SMA and~~ wrote the original first draft, and all. All the authors contributed to ~~its~~ review the interpretation and discussion of the results and in review of the draft.

### **Competing Interests**

The authors declare that they have no conflict of interest.

### **Acknowledgements**

780 SMA is grateful for discussions with Alexandre Tuel and for the text editing by Simon Milligan. OM and SMA acknowledge  
Marco Rohrer for the blocking algorithm. The authors acknowledge the European Centre for Medium-Range Forecasts  
(ECMWF) for producing the ERA-I dataset and the Australian Bureau of Meteorology for producing ACORN-SAT dataset.

### **Funding information**

SMA and OM were funded from the Swiss National Science Foundation grant number 178751. MR was funded from the  
785 INTEXseas project from the European Research Council under the European Union's Horizon 2020 research and innovation  
program (Grant Agreement 787652). KK was partially supported by the NSF project NSF AGS-1934358.

## References

- Ali, M. and Röthlisberger, M.: avatar101/R-metric: (Version v1.1), Zenodo, <https://doi.org/10.5281/zenodo.5742810>, 2021.
- Ali, S. M., Martius, O., and Röthlisberger, M.: Recurrent Rossby Wave Packets Modulate the Persistence of Dry and Wet Spells Across the Globe, *Geophys. Res. Lett.*, 48, e2020GL091452, <https://doi.org/https://doi.org/10.1029/2020GL091452>, 2021.
- 790 Barriopedro, D., Fischer, E. M., Luterbacher, J., Trigo, R. M., and Garcí\`ia-Herrera, R.: The Hot Summer of 2010: Redrawing the Temperature Record Map of Europe, *Science* (80-. ), 332, 220–224, <https://doi.org/10.1126/science.1201224>, 2011.
- Benjamini, Y. and Hochberg, Y.: Controlling the False Discovery Rate: A Practical and Powerful Approach to Multiple Testing, *Source: Journal of the Royal Statistical Society. Series B (Methodological)*, 289–300 pp., 1995.
- 795 Black, E., Blackburn, M., Harrison, G., Hoskins, B., and Methven, J.: Factors contributing to the summer 2003 European heatwave, 59, 217–223, <https://doi.org/10.1256/wea.74.04>, 2004.
- Coumou, D., Robinson, A., and Rahmstorf, S.: Global increase in record-breaking monthly-mean temperatures, *Clim. Change*, 118, 771–782, <https://doi.org/10.1007/s10584-012-0668-1>, 2013.
- Davies, H. C.: Weather chains during the 2013/2014 winter and their significance for seasonal prediction, *Nat. Geosci.*,  
800 <https://doi.org/10.1038/ngeo2561>, 2015.
- Dee, D. P., Uppala, S. M., Simmons, A. J., Berrisford, P., Poli, P., Kobayashi, S., Andrae, U., Balmaseda, M. A., Balsamo, G., Bauer, P., Bechtold, P., Beljaars, A. C. M., van de Berg, L., Bidlot, J., Bormann, N., Delsol, C., Dragani, R., Fuentes, M., Geer, A. J., Haimberger, L., Healy, S. B., Hersbach, H., Hólm, E. V., Isaksen, I., Kållberg, P., Köhler, M., Matricardi, M., McNally, A. P., Monge-Sanz, B. M., Morcrette, J. J., Park, B. K., Peubey, C., de Rosnay, P., Tavolato, C., Thépaut, J. N., and Vitart, F.: The ERA-Interim reanalysis:  
805 Configuration and performance of the data assimilation system, *Q. J. R. Meteorol. Soc.*, 137, 553–597, <https://doi.org/10.1002/qj.828>, 2011.
- Drouard, M. and Woollings, T.: Contrasting Mechanisms of Summer Blocking Over Western Eurasia, *Geophys. Res. Lett.*, 45, 12,040–12,048, <https://doi.org/10.1029/2018GL079894>, 2018.
- Engel CB, Lane TP, Reeder MJ, Rezný M.: The meteorology of Black Saturday, *Q. J. R. Meteorol. Soc.* 139: 585–599,  
810 <https://doi.org/10.1002/qj.1986>, 2013.
- Fragkoulidis, G., Wirth, V., Bossmann, P., and Fink, A. H.: Linking Northern Hemisphere temperature extremes to Rossby wave packets, *Q. J. R. Meteorol. Soc.*, 144, 553–566, <https://doi.org/10.1002/qj.3228>, 2018.
- [Green, J. S. A.: The weather during July 1976: Some dynamical considerations of the drought. \*Weather\*, 32, 120-126, 1977.](#)
- Hoskins, B. J. and Sardeshmukh, P. D.: A Diagnostic Study of the Dynamics of the Northern Hemisphere Winter of 1985-86, *Q. J. R.*

- 815 Meteorol. Soc., 113, 759–778, <https://doi.org/10.1002/qj.49711347705>, 1987.
- Hughes, L., Steffen, W., Mullins, G., Dean, A., Weisbro, E., and Rice, M.: Summer of crisis, 2020.
- Insurance Council Of Australia: INSURANCE COUNCIL OF AUSTRALIA, 2020.
- Karoly D. J.: The recent bushfires and extreme heat wave in southeast Australia. *Bull. Aust. Meteorol. Oceanogr. Soc.*, 22(1):10-3, 2009.
- 820 [King, MJ, Reeder, MJ: Extreme heat events from an object viewpoint with application to south-east Australia. \*Int J Climatol.\*; 41: 2693–2709. <https://doi.org/10.1002/joc.6984>, 2021.](#)
- [Kautz, L.-A., Martius, O., Pfahl, S., Pinto, J. G., Ramos, A. M., Sousa, P. M., and Woollings, T.: Atmospheric blocking and weather extremes over the Euro-Atlantic sector – a review. \*Weather Clim. Dynam.\*, 3, 305–336. <https://doi.org/10.5194/wcd-3-305-2022>, 2022.](#)
- Kornhuber, K., Petoukhov, V., Petri, S., Rahmstorf, S., and Coumou, D.: Evidence for wave resonance as a key mechanism for generating
- 825 high-amplitude quasi-stationary waves in boreal summer. *Clim. Dyn.*, 49, 1961–1979, <https://doi.org/10.1007/s00382-016-3399-6>, 2017a
- [2017.](#)
- [Kornhuber, K., Petoukhov, V., Karoly, D., Petri, S., Rahmstorf, S., Coumou, D.: Summertime Planetary Wave Resonance in the Northern and Southern Hemispheres. \*J. Clim.\*, 30, 6133–6150. <https://doi.org/10.1175/JCLI-D-16-0703.1>, 2017b.](#)
- Kornhuber, K., Coumou, D., Vogel, E., Lesk, C., Donges, J. F., Lehmann, J., and Horton, R. M.: Amplified Rossby waves enhance risk of
- 830 concurrent heatwaves in major breadbasket regions. *Nat. Clim. Chang.*, 10, 48–53, <https://doi.org/10.1038/s41558-019-0637-z>, 2020.
- Martius, O., C. Schwierz, and H. C. Davies.: Tropopause-level waveguides, *J. Atmos.Sci.*, 67, 866–879, <https://doi.org/10.1175/2009JAS2995.1>, 2010.
- [Martius, O., Wehrli, K., & Rohrer, M.: Local and Remote Atmospheric Responses to Soil Moisture Anomalies in Australia. \*Journal of Climate\*, 34\(22\), 9115-9131. <https://doi.org/10.1175/JCLI-D-21-0130.1>, 2021.](#)
- 835 Masson-Delmotte, V., P. Zhai, A. Pirani, S. L., Connors, C. Péan, S. Berger, N. Caud, Y. Chen, L. Goldfarb, M.I. Gomis, M. Huang, K. Leitzell, E. Lonnoy, J. B. R., and Matthews, T.K. Maycock, T. Waterfield, O. Yelekçi, R. Yu, and B. Z. (eds. : IPCC, 2021: Climate Change 2021: The Physical Science Basis. Contribution of Working Group I to the Sixth Assessment Report of the Intergovernmental Panel on Climate Change, <https://www.ipcc.ch/report/ar6/wg1/#FullReport>, 2021.
- National Climate Centre (2004) Eastern Australia experiences record February heatwave. *Bull. Aust. Meteorol. Oceanogr Soc.* 17:27–29
- 840 O'Brien, L. and Reeder, M. J.: Southern Hemisphere summertime Rossby waves and weather in the Australian region, *Q. J. R. Meteorol. Soc.*, 143, 2374–2388, <https://doi.org/10.1002/qj.3090>, 2017.
- Parker, T., Berry, G. J., Reeder, M. J., and Nicholls, N.: Modes of climate variability and heat waves in Victoria, southeastern Australia, *Geophys. Res. Lett.*, 41, 6926–6934, <https://doi.org/10.1002/2014GL061736>, 2014a.
- Parker, T., Berry, G. J., Reeder, M. J., Berry, G. J., and Reeder, M. J.: The Structure and Evolution of Heat Waves in Southeastern



- 845 Australia, *J. Clim.*, 27, 5768–5785, <https://doi.org/10.1175/JCLI-D-13-00740.1>, 2014b.
- Parker, T., Quinting, J., and Reeder, M.: The synoptic-dynamics of summertime heatwaves in the Sydney area (Australia), *J. South. Hemisph. Earth Syst. Sci.*, 69, 116, <https://doi.org/10.1071/es19004>, 2019.
- Pelly, J. L., & Hoskins, B. J.: A New Perspective on Blocking, *Journal of the Atmospheric Sciences*, 60(5), 743-755, [https://doi.org/10.1175/1520-0469\(2003\)060<0743:ANPOB>2.0.CO;2](https://doi.org/10.1175/1520-0469(2003)060<0743:ANPOB>2.0.CO;2), 2003.
- 850 Perkins-Kirkpatrick, S. E. and Lewis, S. C.: Increasing trends in regional heatwaves, *Nat. Commun.*, 11, 1–8, 2020.
- Petoukhov, V., Rahmstorf, S., Petri, S., and Schellnhuber, H. J.: Quasiresonant amplification of planetary waves and recent Northern Hemisphere weather extremes, *Proc. Natl. Acad. Sci. U. S. A.*, 110, 5336–5341, <https://doi.org/10.1073/pnas.1222000110>, 2013.
- Pfahl, S. and Wernli, H.: Quantifying the relevance of atmospheric blocking for co-located temperature extremes in the Northern Hemisphere on (sub-)daily time scales, *Geophys. Res. Lett.*, 39, 1–6, <https://doi.org/10.1029/2012GL052261>, 2012.
- 855 Quandt, L.-A., Keller, J. H., Martius, O., and Jones, S. C.: Forecast variability of the blocking system over Russia in summer 2010 and its impact on surface conditions, *Weather Forecast.*, 32, 61–82, 2017.
- Quinting, J. F., Reeder, M. ~~J.~~, ~~Quinting, J. F., and Reeder, M. J.~~: Southeastern Australian Heat Waves from a Trajectory Viewpoint, *Mon. Weather Rev.*, 145, 4109–4125, <https://doi.org/10.1175/MWR-D-17-0165.1>, 2017.
- ~~Risbey, J. S., O’Kane, T. J., Monselesan, D. P., Franzke, C. L. E., & Horenko, I. On the dynamics of Austral heat waves. *Journ. of*~~
- 860 ~~*Geophys. Res.: Atmos.*, 123, 38– 57. <https://doi.org/10.1002/2017JD027222>, 2018.~~
- Rohrer, M., Brönnimann, S., Martius, O., Raible, C. C., Wild, M., and Compo, G. P.: Representation of extratropical cyclones, blocking anticyclones, and alpine circulation types in multiple reanalyses and model simulations, *J. Clim.*, 31, 3009–3031, <https://doi.org/10.1175/JCLI-D-17-0350.1>, 2018.
- Röthlisberger, M., Frossard, L., Bosart, L. F., Keyser, D., and Martius, O.: Recurrent synoptic-scale Rossby wave patterns and their effect
- 865 on the persistence of cold and hot spells, *J. Clim.*, 32, 3207–3226, <https://doi.org/10.1175/JCLI-D-18-0664.1>, 2019.
- Schneiderreit, A., Schubert, S., Vargin, P., Lunkeit, F., Zhu, X., Peters, D. H. W., and Fraedrich, K.: Large-Scale Flow and the Long-Lasting Blocking High over Russia: Summer 2010, *Mon. Weather Rev.*, 140, 2967–2981, <https://doi.org/10.1175/MWR-D-11-00249.1>, 2012.
- Schwierz, C., Croci-Maspoli, M., and Davies, H. C.: Perspicacious indicators of atmospheric blocking, *Geophys. Res. Lett.*, 31, ~~n/a-n/a~~6, <https://doi.org/10.1029/2003gl019341>, 2004.
- 870 ~~*Seneviratne, S.I., Corti, T., Davin, E.L., Hirschi, M., Jaeger, E.B., Lehner, I., Orlowsky, B. and Teuling, A.J.: Investigating soil moisture–climate interactions in a changing climate: A review. *Earth-Science Reviews*, 99(3-4), pp.125-161., 2010.*~~

- Shepherd, T. G.: Atmospheric circulation as a source of uncertainty in climate change projections, *Nat. Geosci.*, 7, 703–708, <https://doi.org/10.1038/NGEO2253>, 2014.
- 875 Shutts, G. J.: The propagation of eddies in diffluent jetstreams: Eddy vorticity forcing of ‘blocking’ flow fields, *Q. J. R. Meteorol. Soc.*, <https://doi.org/10.1002/qj.49710946204>, 1983.
- Sousa, P. M., D. Barriopedro, R. García-Herrera, T. Woollings, and R. M. Trigo: A new combined detection algorithm for blocking and subtropical ridges, *J. Clim.*, 34, 18, 7735–7758, <https://doi.org/10.1175/JCLI-D-20-0658.1>, 2021.
- Teng, H., Branstator, G., Meehl, G. A., and Washington, W. M.: Projected intensification of subseasonal temperature variability and heat waves in the Great Plains, *Geophys. Res. Lett.*, 43, 2165–2173, <https://doi.org/https://doi.org/10.1002/2015GL067574>, 2016.
- 880 Trigo, R. M., Trigo, I. F., DaCamara, C. C., and Osborn, T. J.: Climate impact of the European winter blocking episodes from the NCEP/NCAR Reanalyses, *Clim. Dyn.*, 23, 17–28, <https://doi.org/10.1007/s00382-004-0410-4>, 2004.
- VBRC: Final report of the Victorian Bushfires Royal Commission. [Available online at <http://www.royalcommission.vic.gov.au/Commission-Reports>.], 2010.
- 885 Wehrli, K., Guillod, B. P., Hauser, M., Leclair, M., and Seneviratne, S. I.: Identifying Key Driving Processes of Major Recent Heat Waves, *J. Geophys. Res. Atmos.*, 124, 11746–11765, <https://doi.org/https://doi.org/10.1029/2019JD030635>, 2019.
- Wernli, H. and Schwierz, C.: Surface cyclones in the ERA-40 dataset (1958–2001). Part I: Novel identification method and global climatology, *J. Atmos. Sci.*, 63, 2486–2507, <https://doi.org/10.1175/JAS3766.1>, 2006.
- White, R. H., Kornhuber, K., Martius, O., and Wirth, V.: From Atmospheric Waves to Heatwaves: A Waveguide Perspective for Understanding and Predicting Concurrent, Persistent and Extreme Extratropical Weather, *Bull. Am. Meteorol. Soc.*, 1–35, <https://doi.org/10.1175/BAMS-D-21-0170.1>, 2021.
- 890 Wilks, D. S.: “The stippling shows statistically significant grid points”: How research results are routinely overstated and overinterpreted, and what to do about it, <https://doi.org/10.1175/BAMS-D-15-00267.1>, 2016.
- Wirth, V.: ~~Waveguidability of idealized midlatitude jets and the limitations of ray tracing theory, *Weather Clim. Dyn.*, 1, 111–125, <https://doi.org/10.5194/wcd-1-111-2020>, 2020.~~
- 895 ~~Wirth, V. and Polster, C.: The problem of diagnosing jet waveguidability in the presence of large-amplitude eddies, *J. Atmos. Sci.*, 3137–3151, <https://doi.org/10.1175/jas-d-20-0292.1>, 2021.~~
- ~~Wirth, V., Riemer, M., Chang, E. K. M., and Martius, O.: Rossby Wave Packets on the Midlatitude Waveguide — A Review, *Mon. Weather Rev.*, MWR-D-16-0483.1, <https://doi.org/10.1175/MWR-D-16-0483.1>, 2018.~~
- 900 Zimin, A. V., Szunyogh, I., Patil, D. J., Hunt, B. R., and Ott, E.: Extracting Envelopes of Rossby Wave Packets, *Mon. Weather Rev.*,

[https://doi.org/10.1175/1520-0493\(2003\)131<1011:EEORWP>2.0.CO;2](https://doi.org/10.1175/1520-0493(2003)131<1011:EEORWP>2.0.CO;2), 2003.

[Wolf, G., Brayshaw, D.J., Klingaman, N.P. and Czaja, A.: Quasi-stationary waves and their impact on European weather and extreme events. \*Quarterly Journal of the Royal Meteorological Society\*, 144\(717\), pp.2431-2448, 2018.](#)

**Formatted:** Font: 9 pt